

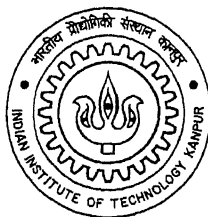
# **Effect of Thermomechanical Treatment on the Microstructural Evolution of 38MnSiV6 Microalloyed Steel**

A Thesis  
Submitted by

**Garima Khanna**

for the award of the degree of

**Master of Technology**

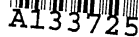


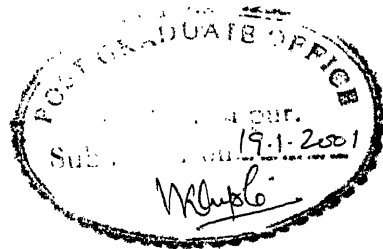
**Department of Materials and Metallurgy Engineering  
Indian Institute of Technology  
Kanpur**

January 2001

अवधि-१३३७२५

1. 2. 3. 4. 5. 6. 7. 8. 9. 10. 11. 12. 13. 14. 15. 16. 17. 18. 19. 20. 21. 22. 23. 24. 25. 26. 27. 28. 29. 30. 31. 32. 33. 34. 35. 36. 37. 38. 39. 40. 41. 42. 43. 44. 45. 46. 47. 48. 49. 50. 51. 52. 53. 54. 55. 56. 57. 58. 59. 60. 61. 62. 63. 64. 65. 66. 67. 68. 69. 70. 71. 72. 73. 74. 75. 76. 77. 78. 79. 80. 81. 82. 83. 84. 85. 86. 87. 88. 89. 90. 91. 92. 93. 94. 95. 96. 97. 98. 99. 100. 101. 102. 103. 104. 105. 106. 107. 108. 109. 110. 111. 112. 113. 114. 115. 116. 117. 118. 119. 120. 121. 122. 123. 124. 125. 126. 127. 128. 129. 130. 131. 132. 133. 134. 135. 136. 137. 138. 139. 140. 141. 142. 143. 144. 145. 146. 147. 148. 149. 150. 151. 152. 153. 154. 155. 156. 157. 158. 159. 160. 161. 162. 163. 164. 165. 166. 167. 168. 169. 170. 171. 172. 173. 174. 175. 176. 177. 178. 179. 180. 181. 182. 183. 184. 185. 186. 187. 188. 189. 190. 191. 192. 193. 194. 195. 196. 197. 198. 199. 200. 201. 202. 203. 204. 205. 206. 207. 208. 209. 210. 211. 212. 213. 214. 215. 216. 217. 218. 219. 220. 221. 222. 223. 224. 225. 226. 227. 228. 229. 230. 231. 232. 233. 234. 235. 236. 237. 238. 239. 240. 241. 242. 243. 244. 245. 246. 247. 248. 249. 250. 251. 252. 253. 254. 255. 256. 257. 258. 259. 260. 261. 262. 263. 264. 265. 266. 267. 268. 269. 270. 271. 272. 273. 274. 275. 276. 277. 278. 279. 280. 281. 282. 283. 284. 285. 286. 287. 288. 289. 290. 291. 292. 293. 294. 295. 296. 297. 298. 299. 300. 301. 302. 303. 304. 305. 306. 307. 308. 309. 310. 311. 312. 313. 314. 315. 316. 317. 318. 319. 320. 321. 322. 323. 324. 325. 326. 327. 328. 329. 330. 331. 332. 333. 334. 335. 336. 337. 338. 339. 340. 341. 342. 343. 344. 345. 346. 347. 348. 349. 350. 351. 352. 353. 354. 355. 356. 357. 358. 359. 360. 361. 362. 363. 364. 365. 366. 367. 368. 369. 370. 371. 372. 373. 374. 375. 376. 377. 378. 379. 380. 381. 382. 383. 384. 385. 386. 387. 388. 389. 390. 391. 392. 393. 394. 395. 396. 397. 398. 399. 400. 401. 402. 403. 404. 405. 406. 407. 408. 409. 410. 411. 412. 413. 414. 415. 416. 417. 418. 419. 420. 421. 422. 423. 424. 425. 426. 427. 428. 429. 430. 431. 432. 433. 434. 435. 436. 437. 438. 439. 440. 441. 442. 443. 444. 445. 446. 447. 448. 449. 450. 451. 452. 453. 454. 455. 456. 457. 458. 459. 460. 461. 462. 463. 464. 465. 466. 467. 468. 469. 470. 471. 472. 473. 474. 475. 476. 477. 478. 479. 480. 481. 482. 483. 484. 485. 486. 487. 488. 489. 490. 491. 492. 493. 494. 495. 496. 497. 498. 499. 500. 501. 502. 503. 504. 505. 506. 507. 508. 509. 510. 511. 512. 513. 514. 515. 516. 517. 518. 519. 520. 521. 522. 523. 524. 525. 526. 527. 528. 529. 530. 531. 532. 533. 534. 535. 536. 537. 538. 539. 540. 541. 542. 543. 544. 545. 546. 547. 548. 549. 550. 551. 552. 553. 554. 555. 556. 557. 558. 559. 560. 561. 562. 563. 564. 565. 566. 567. 568. 569. 570. 571. 572. 573. 574. 575. 576. 577. 578. 579. 580. 581. 582. 583. 584. 585. 586. 587. 588. 589. 590. 591. 592. 593. 594. 595. 596. 597. 598. 599. 600. 601. 602. 603. 604. 605. 606. 607. 608. 609. 610. 611. 612. 613. 614. 615. 616. 617. 618. 619. 620. 621. 622. 623. 624. 625. 626. 627. 628. 629. 630. 631. 632. 633. 634. 635. 636. 637. 638. 639. 640. 641. 642. 643. 644. 645. 646. 647. 648. 649. 650. 651. 652. 653. 654. 655. 656. 657. 658. 659. 660. 661. 662. 663. 664. 665. 666. 667. 668. 669. 670. 671. 672. 673. 674. 675. 676. 677. 678. 679. 680. 681. 682. 683. 684. 685. 686. 687. 688. 689. 690. 691. 692. 693. 694. 695. 696. 697. 698. 699. 700. 701. 702. 703. 704. 705. 706. 707. 708. 709. 710. 711. 712. 713. 714. 715. 716. 717. 718. 719. 720. 721. 722. 723. 724. 725. 726. 727. 728. 729. 730. 731. 732. 733. 734. 735. 736. 737. 738. 739. 740. 741. 742. 743. 744. 745. 746. 747. 748. 749. 750. 751. 752. 753. 754. 755. 756. 757. 758. 759. 760. 761. 762. 763. 764. 765. 766. 767. 768. 769. 770. 771. 772. 773. 774. 775. 776. 777. 778. 779. 780. 781. 782. 783. 784. 785. 786. 787. 788. 789. 790. 791. 792. 793. 794. 795. 796. 797. 798. 799. 800. 801. 802. 803. 804. 805. 806. 807. 808. 809. 810. 811. 812. 813. 814. 815. 816. 817. 818. 819. 820. 821. 822. 823. 824. 825. 826. 827. 828. 829. 830. 831. 832. 833. 834. 835. 836. 837. 838. 839. 840. 84





## Certificate

This is to certify that the thesis entitled "**Effect of Thermomechanical Treatment on the Evolution of Microstructure of 38MnSiVS6** " submitted by Ms.Garima Khanna (Roll No. 9910610) to the Indian Institute of Technology, Kanpur for the award of Master of Technology is a bonafide record of research work carried out under my supervision. The contents of this, in full or in parts, have not been submitted to any other institute or university for the award of any degree or diploma.

A handwritten signature in black ink, appearing to read "Sandeep Sangal".

Dr. Sandeep Sangal

Research Guide

Department of Materials and Metallurgical Engineering

Indian Institute of Technology

Kanpur-208016, India

Date: January 2001

## Acknowledgements

I would like to express my deep sense of gratitude and sincere thanks to **Dr. Sandeep Sangal**, my research guide, for helpful guidance and constant encouragement. It has been his ever-helping attitude that has made this work possible.

I am very highly indebted to **Dr. M.N.Mungole** for his invaluable help. His assistance in the general course of this investigation is also deeply acknowledged.

I express my sincere thanks to **Mr. B.K. Jain**, lab in-charge Materials Testing lab, for his invaluable help in carrying out tensile tests and micro hardness measurements.

I wish to thank **Mr. H.C. Srivastava** for letting me use the sample-cutting machine and furnace facility of the Heat treatment lab.

I am grateful to **Mr. Agnihotri** and **Mr. R.P. Singh** for their help in carrying out SEM and EPMA investigation. I also thank **Mr. Uma Shankar** for his help in carrying out X-ray diffraction.

I wish to thank **Mr. Sharma**, Metallurgical workshop, for making tensile samples.

I also thank **Mr. Murli**, assistant in Physical Metallurgy lab, for his help in various stages of sample preparation.

I am grateful to **Dr. Gouthama** and **Mr. A.K.Sahoo** for helping me during the last stages of my work.

I have great pleasure in thanking **Mr. S.Sankaran**, my fellow research scholar, for providing a jovial atmosphere, valuable suggestions and stimulating discussion.

Last but not the least, I would like to acknowledge the affection, respect and support received from my friends, **Ms. Swagatika Mohapatra** and **Ms. Payal Jain**. Their company has made my stay in IITK a memorable one.

## Abstract

Microalloyed medium carbon steels are increasingly being used with a new post forging two-step cooling sequence, which acts as an alternative to the quenched and tempered route. This leads to the elimination of the need to subsequently heat-treat, straighten and stress relieve that reduces the costs. This thesis deals with the microstructural study of a medium carbon microalloyed steel (38MnSiVS6) that has been thermomechanically treated with varying deformation and cooling sequences. The main objective is to describe the development of the microstructure after forging followed by two-step cooling and annealing treatment and its dependence on the variation of process parameters along with the microalloying additions. The relationship between the microstructure and the resulting mechanical properties are also explored.

The microalloying content along with the parameters of thermomechanical treatment play a very significant role in obtaining the final microstructure and also the final mechanical properties. 38MnSiVS6 medium carbon microalloyed steel was subjected to varying thermomechanical treatment, which led to a variation in microstructure obtained. The microstructure was qualitatively and quantitatively identified and compared with respect to variation in deformation temperature and cooling sequence. The two-step cooled material was studied and compared with the continuously cooled material. The impact of change in annealing temperature and annealing time on annealing of two-step cooled material was related to the microstructure and the mechanical properties of the material. The optimum annealing temperature and time was also identified by correlating it to the best tensile properties that were obtained. The differently treated samples were subjected to X-ray diffraction to identify the phases present in the structure and their volume fraction.

The two-step cooled structure showed lower bainite and free ferrite as compared to ferrite pearlite structure of continuously cooled material. The variation in grain size of the structure and the variation in volume fraction of proeutectoid ferrite along the length

of forged rod (initial length) were related to the gradient in cooling rate. Due to change in cooling rate different sections of the rod are being forged at different temperatures. This resulted in a minimum in ferrite fraction and maxima in grain size along all differently treated rods. The importance of decrease in deformation temperature for two-step cooled sample was confirmed. The material deformed at lower finish forging temperature (TSC2) had higher content of ferrite and the structure was finer than in TSC1, the two-step cooled material finished forged at a higher temperature. The TSC2 material also had higher hardness values than the TSC1 and this led to high strength levels along with improved ductility due to increased free ferrite fraction. The variation in annealing temperature and annealing time during annealing did not signify any variation in the microstructural observation and the hardness. But it was observed that optimum tensile properties are obtained for the TSC2 material annealed at 450°C for 1.5 hrs. Hence the duplex microstructure consisting of soft ferrite along with hard bainite has been found to be the optimum microstructure that gives good properties.

# Contents

|   |           |
|---|-----------|
| <b>Certificate</b>  |           |
| <b>Acknowledgements</b>                                       | (i)       |
| <b>Abstract</b>   | (ii)      |
| <b>Contents</b>   | (iv)      |
| <b>List of Figures</b>  | (vi)      |
| <b>List of tables</b>   | (vii)     |
| <b>1. INTRODUCTION</b>  | <b>1</b>  |
| 1.1. Continuous Cooling (CC): An Alternative to QT – Route    | 1         |
| 1.2 Two Step Cooling: Controlling Parameters                  | 2         |
| 1.3 Annealing After Two Step Cooling Treatment                | 6         |
| 1.4 Objectives of Present Investigation                       | 8         |
| <b>2. LITERATURE REVIEW</b>                                   | <b>9</b>  |
| 2.1 Microalloying Elements                                    | 10        |
| 2.1.1 Solubility Product                                      | 10        |
| 2.1.2 Retardation of Austenite ( $\gamma$ ) Recrystallization | 12        |
| 2.1.3 Grain Refinement and Precipitation Hardening            | 13        |
| 2.2 Microstructures in Steel                                  | 13        |
| 2.2.1 Cementite ( $\text{Fe}_3\text{C}$ )                     | 13        |
| 2.2.2 Ferrite ( $\alpha$ )                                    | 14        |
| 2.2.3 Pearlite  | 15        |
| 2.2.4 Martensite  | 17        |
| 2.2.5 Bainite   | 21        |
| <b>3. EXPERIMENTAL PROCEDURE</b>                              | <b>30</b> |
| 3.1 Starting Material   | 30        |
| 3.2 Thermomechanical Processing                               | 30        |
| 3.3 Quantitative Microscopy                                   | 32        |
| 3.3.1 Sample Preparation                                      | 33        |
| 3.3.2 Optical Microscopy                                      | 33        |

|           |                                      |           |
|-----------|--------------------------------------|-----------|
| 3.3.3     | Scanning Electron Microscopy         | 34        |
| 3.4       | Stereological Measurements           | 34        |
| 3.5       | X-Ray Diffraction                    | 35        |
| 3.6       | Mechanical Testing                   | 39        |
| 3.6.1     | Hardness Measurements                | 39        |
| 3.6.2     | Tensile Testing                      | 40        |
| <b>4.</b> | <b>RESULTS AND DISCUSSIONS</b>       | <b>41</b> |
| 4.1       | Microstructure                       | 41        |
| 4.1.1     | Air-Cooled Material                  | 41        |
| 4.1.2     | Two-Step Cooled Material             | 46        |
| 4.1.3     | Annealed Structure o Two-Step Cooled | 55        |
| 4.2       | Stereological Measurements           | 57        |
| 4.3       | X-Ray Diffraction Results            | 63        |
| 4.4       | Mechanical Testing Results           | 69        |
| 4.4.1     | Hardness Measurements                | 69        |
| 4.4.2     | Tensile Tests                        | 72        |
| <b>5.</b> | <b>CONCLUSIONS</b>                   | <b>79</b> |
|           | Conclusions                          | 79        |
|           | Suggestions For Future Work          | 80        |
|           | References                           | 81        |



## List of Figures

- Figure 1.1 Effect of Deformation Temperature  $T_D$  on the Specimen Hardness HV10 and on microhardness.
- Figure 1.2 Mechanical Properties of Forged and Continuously Cooled Compared with Conventional QT Treatment.
- Figure 1.3 Processing Schedules for the Two-Step Cooling Treatment.
- Figure 1.4 Comparison of Mechanical Properties of Two-Step Cooled with QT Treatment.
- Figure 1.5 Influence of an Additional Treatment on the Stress Strain Curve of Two-Step cooled steel.
- Figure 2.1 Solubility Products of carbides and nitrides in austenite.
- Figure 2.2 Schematic Diagram Illustrating the Combined Effect of Lattice Deformation and Lattice Invariant Deformation
- Figure 2.3 Schematic Diagram Illustrating Two Types of Lattice Deformation: Slip and Twin
- Figure 2.4 Schematic Diagram Illustrating the Difference in the Shape of Pearlite and Bainite
- Figure 2.5 Schematic Diagram Illustrating the Microstructural Factors Relevant in the Kinetic Description of Bainite.
- Figure 2.6 Effect of Carbon Content on the Temperature for Transition from Upper to Lower Bainite.
- Figure 2.7 Schematic Representation of the Transition from Upper to Lower Bainite
- Figure 3.1 Thermomechanical Treatment Cycle for 38MnSiVS6
- Figure 4.1 Microstructure of Air-Cooled Samples
- Figure 4.2 Microstructure of Air-Cooled Samples
- Figure 4.3 Microstructure of Air-Cooled Samples at 10,000X
- Figure 4.4 Microstructure of Two-Step Cooled Samples Taken from Extreme End of the Rod.
- Figure 4.5 Microstructure of Two-Step Cooled Material at 1000X
- Figure 4.6 Microstructures of TSC1 at 5000X

- Figure 4.7 Comparison of Microstructures of TSC1 And TSC2
- Figure 4.8 Microstructures of TSC2 At 8,000X
- Figure 4.9 Microstructures of TSC2 At 10,000X
- Figure 4.10 Microstructure of Annealed Two–Step Cooled Material at 1000X
- Figure 4.11 Microstructure of Two – Step Cooled Samples Annealed at 450° C For 1.5 Hrs.
- Figure 4.12 SEM Micrographs of Annealed TSC2
- Figure 4.13 Microstructures of Annealed Two – Step Cooled Samples
- Figure 4.14 Variation of Proeutectoid Ferrite Content along the Length of Rod
- Figure 4.15 Variation Of Cementite (in Bainite) along the Length of Rod
- Figure 4.16 Variation in Surface Area Per Unit Volume of Cementite Along the Rod.
- Figure 4.17 Representative X-Ray Diffraction Plot of Two-Step Cooled Sample.
- Figure 4.18 Variation of Hardness(RC) along the Length of the Thermomechanically Treated Rod.
- Figure 4.19 Variation in Hardness of Two-Step Cooled Samples along the length of the Rod.
- Figure 4.20 Variation in Hardness, Strength and Ductility with Variation in Annealing Temperature.
- Figure 4.21 Representative Engineering Stress-Strain Curve

## List of Tables

|           |  |
|-----------|--|
| Table 3.1 | Chemical Composition of 38MnSiVS6.   |
| Table 3.2 | Coordinates of Atoms of Cementite.   |
| Table 3.2 | Theoretical intensities Obtained with Cu-K $\alpha$ Radiation at different hkl planes.                     |
| Table 4.1 | Variation of Interlamellar Spacing along the Length of the Rod.  |
| Table 4.2 | Peaks Observed at 2 $\theta$ for Cementite and Ferrite.  |
| Table 4.3 | Volume Fraction of Cementite as Obtained with X-Ray Diffraction.   |
| Table 4.3 | Comparison of Hardness of Two-Step Cooled Condition.   |
| Table 4.4 | Comparison of Toughness of Optimal Two-step Cooled Condition with Optimal Quenched and Tempered Condition. |
| Table 4.5 | Tensile Properties of Different Conditions   |

# Chapter 1

## INTRODUCTION

These days focus is on new materials with improved mechanical properties, reduced weight and realizing cost-effective manufacturing. Microalloyed forging steels have been developed to improve the competitiveness of wrought steel components, especially in the automotive sector, achieving the desired properties in the as forged condition [1]. Microalloyed steel has proven to be a very important material as it can provide a higher strength with smaller alloying additions and less heat treatment expenses. Quenching followed by tempering (QT) has been the conventional route but it requires expensive straightening and stress relieving cycles and also has high product rejection. The attempt to overcome these difficulties led to the introduction of continuous cooling (CC) of medium carbon microalloyed steels from the forging temperature producing a ferritic-pearlitic microstructure in the products. Therefore, first the continuous cooling treatment and the reasons for its failure are discussed. This is followed by discussion on a new post forging treatment, two-step cooling (TSC), which was introduced as a substitute to CC.

### 1.1

#### **Continuous Cooling (CC): An Alternative to QT-Route**

Quenching and tempering (QT) has been the conventional route for obtaining the desired mechanical properties in steels. Due to various technical and economical shortcomings associated with QT treatment, continuous cooling (CC) from the forging temperature was introduced as its alternative [2]. In this treatment desired changes in the microstructure are accomplished through controlled variations in the cooling rate. By control of the cooling rate, fineness of pearlite can be controlled and hardness values comparable to that obtained by QT treatment can be achieved [2].

The deformation temperature is also a very important parameter. Decrease in the deformation temperature has long been known to bring about an increase in the strength value. It is also certain that lowering the deformation temperature will increase the ferrite fraction formed (the softer phase) aided by the increase in the nucleation sites in the unrecrystallised austenite. These two opposing observations of raised strength levels along with an increase in amount of softer ferrite, is related to the hardness obtained. It was observed by the microhardness measurement that higher individual phase hardness, is shown by the sample deformed at lower temperature as shown in (figure 1.1) [3]. This accounts for the high strength level in the sample deformed at lower temperature. The ferrite formed is deformation induced; hence it forms at comparatively higher temperature having high carbon content and shows higher hardness.

The mechanical properties obtained by continuous cooling (CC) are compared with those measured on QT treated specimens, shown as hatched area in figure 1.2. It can be seen that values of ultimate tensile strength (UTS) obtained after QT is achievable after CC. But values of yield strength (YS) and reduction in area (RA) is clearly worse over the whole range of cooling rates. By increasing cooling rate, strength is seen to be increasing because of increase in pearlite to ferrite volume ratio. More over increase in cooling rate decreases the pearlite transformation temperature, which decreases the interlamellar pearlitic spacing and increases strength. It has been observed that further increase in cooling rate decreases the ferrite fraction and promotes bainite formation at the cost of pearlite [3]. This leads to an over all increase in strength and significant drop in ductility. It can be seen from figure 1.2 that there exists no convenient cooling rate, which gives satisfactory YS, and RA values, which are achievable, by QT treatment. This led to failure of continuous cooling treatment and made introduction of two-step cooling a very necessary move.

## 1.2

### **Two-Step Cooling: Controlling Parameters.**

In two-step cooling process, two different cooling rates are involved after the forging treatment as shown in figure 1.3. The first slow cooling step (with cooling rate T1) leads to formation of ferrite. The deformation induced ferrite forms at comparatively high

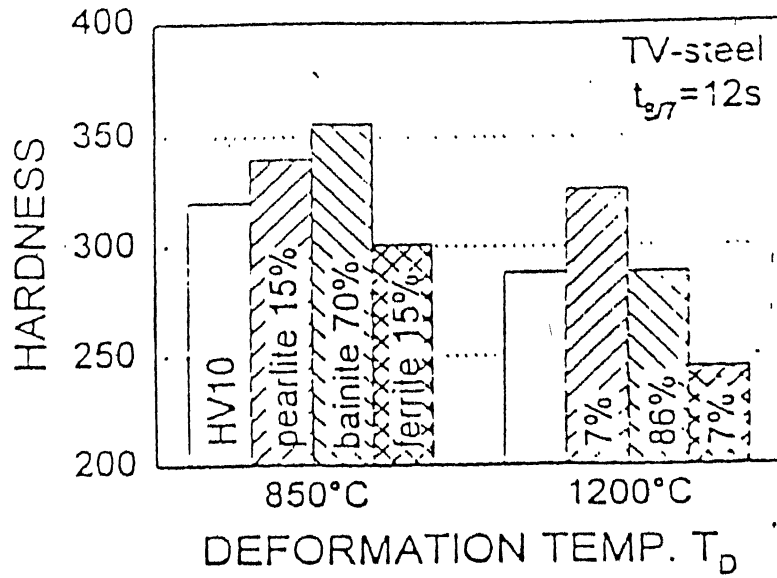


Figure 1.1: Effect of Deformation Temperature on the specimen hardness HV10 and on Microhardness.

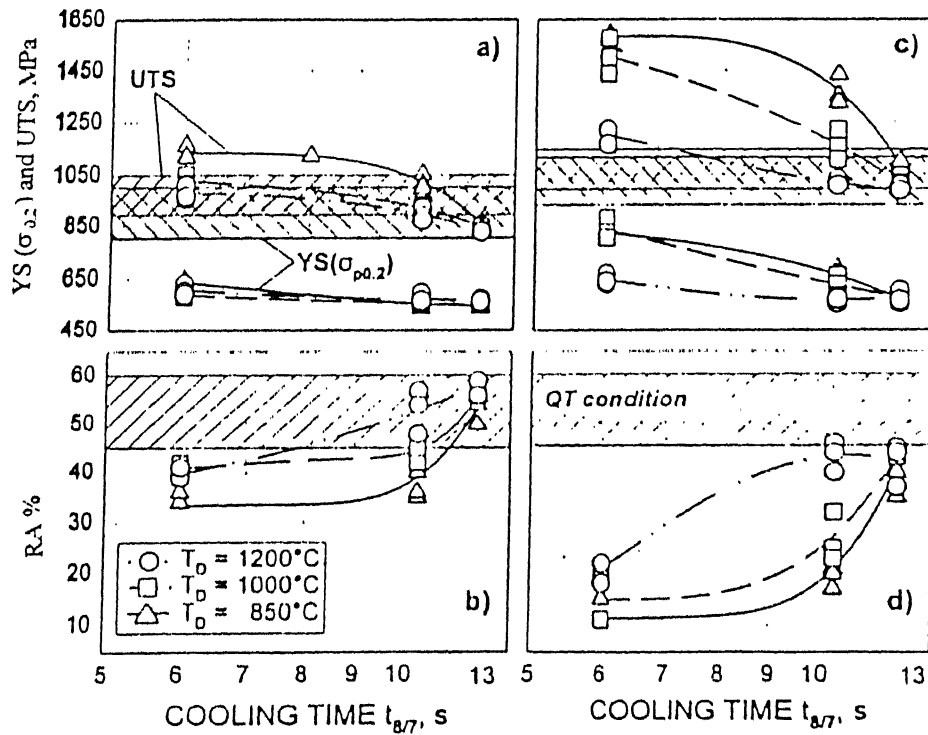


Figure 1.2: Mechanical Properties of Continuously Cooled Treatment with Quenched and Tempered Treatment.

consequently ferrite is polygonal and has higher carbon in it. This gives better toughness and also higher strength because of high carbon content. More over at high temperature, the supersaturated carbon in ferrite diffuses and stabilizes the adjacent austenite. This suppresses pearlitic transformation and as a consequence aids the bainitic formation. The second cooling step (cooling rate  $T_2$ ), of accelerated kind, leads to the formation of harder phases such as bainite and martensite [4].

The volume fractions of both soft and hard, phases in the microstructure is function of forging temperature ( $T_D$ ) and the quenching temperature ( $T_Q$ ). By lowering  $T_Q$  the time available for ferrite formation is increased and thus the volume of softer phase increases. In the same way if  $T_D$  is decreased, finer recrystallised austenite grains or if possible even unrecrystallised grains are obtained, in consequence increasing the ferrite nucleation sites and its volume fraction. The ferrite nucleation rate is also known to increase because of the increase in the defect density near the austenite grain boundaries and ferrite nucleation also occurs on deformation bands within the unrecrystallised grains. With decreased  $T_D$ , high hardness is obtained in spite of increased amount of softer phase, ferrite, having formed because of the reasons explained in section 1.1 [3-5].

Mechanical properties after low temperature deformation and two-step cooling are compared with those obtained after QT and are shown in figure 1.4 [5]. The formation of harder, bainite or martensite, phases has increased the UTS but 0.2% proof stress ( $\sigma_{P 0.2}$ ) and ductility (RA) are quite poor. The low 0.2% proof stress has been attributed to the production of mobile dislocations in ferrite, close to the ferrite-martensite interface, during the austenite to martensite transformation (due to volume expansion). So free dislocations are not locked through atmospheric interstitial solutes. This makes initial plastic deformation easier and discontinuous yielding of the steel is avoided and as a result lower  $\sigma_{P 0.2}$  is obtained [2-3]. Poor ductility after TSC is because of the presence of untempered harder bainite/martensite phase. It was concluded that TSC treatment by itself was no way superior to either QT or CC treatment but in conjugation with an additional annealing treatment it showed comparative tensile properties.

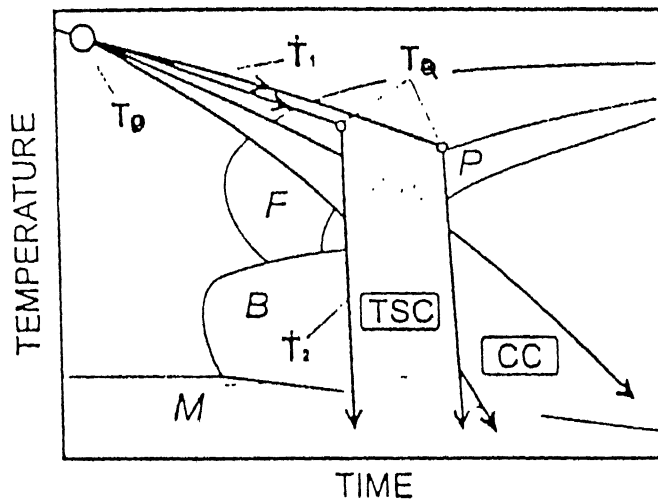


Figure 1.3: Processing Schedules for the Two-Step Cooling.

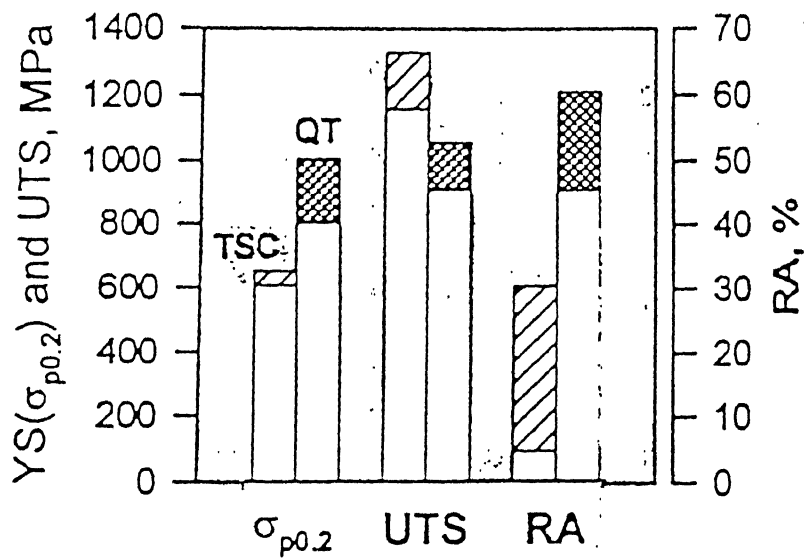


Figure 1.4: Comparison of Mechanical Properties of Two-Step Cooled Treatment with Quenching and Tempering Treatment.



### 1.3

#### Annealing After Two-Step Cooling Treatment.

Annealing has been shown to be very necessary after the two-step cooling treatment for obtaining good mechanical properties. It brings significant changes in the initial part of stress strain curve as shown in figure 1.5. The absence of discontinuous yielding in the unannealed samples and its presence with Luders strain in annealed samples is quite prominent [3]. Annealing treatment leads to an increase in  $\sigma_{P\ 0.2}$ , which can be related to the pinning effect of the interstitial atoms [4-5] and also to the precipitation of vanadium carbonitrides from supersaturated ferrite, preferably in high dislocation density regions. Increase in strength can also be related to decomposition of retained austenite, to carbides and ferrite, in the annealing temperature range. Simultaneously, the increase in ductility is also because of the tempering of bainite (or martensite) phase. It can be seen from figure 1.6 that there is a linear increase in  $\sigma_{P\ 0.2} / \text{UTS}$  value from 0.5 (without annealing) up to 0.85 (after annealing). It can be observed in figure 1.4 that UTS for annealed two step cooled samples is higher than for the QT samples over the whole range of annealing temperatures and there exists a very wide range of  $T_{AN}$  at which yield strength and ductility values are comparable to QT values.

The toughness of the TSC treated steel has been studied by Charpy test and was compared with QT steel. It has been observed that medium carbon steels, irrespective of being given TSC or QT treatment, show lower toughness properties than the QT alloyed steel. Various alloying elements like Cr, Mo and W result in fine dispersion of stable carbides during annealing at the temperature range of 500-600°C. The precipitation of stable carbides influences the precipitation kinetics of iron carbides. This reduces the embrittlement induced by the preferential formation of iron carbides on former grain boundaries and martensite needles, as continuous net and consequently improving the toughness properties [3]. By optimizing TSC processing conditions satisfactory toughness properties can be attained. So the ferrite microstructure obtained after TSC treatment not only gives good strength and ductility but also decent toughness properties. It has been found out that the upper shelf energy and the impact transition temperature of TSC- treated steels improve linearly with the ferrite volume fraction. Hence TSC combined with annealing treatment is preferred over the QT and CC treatment.

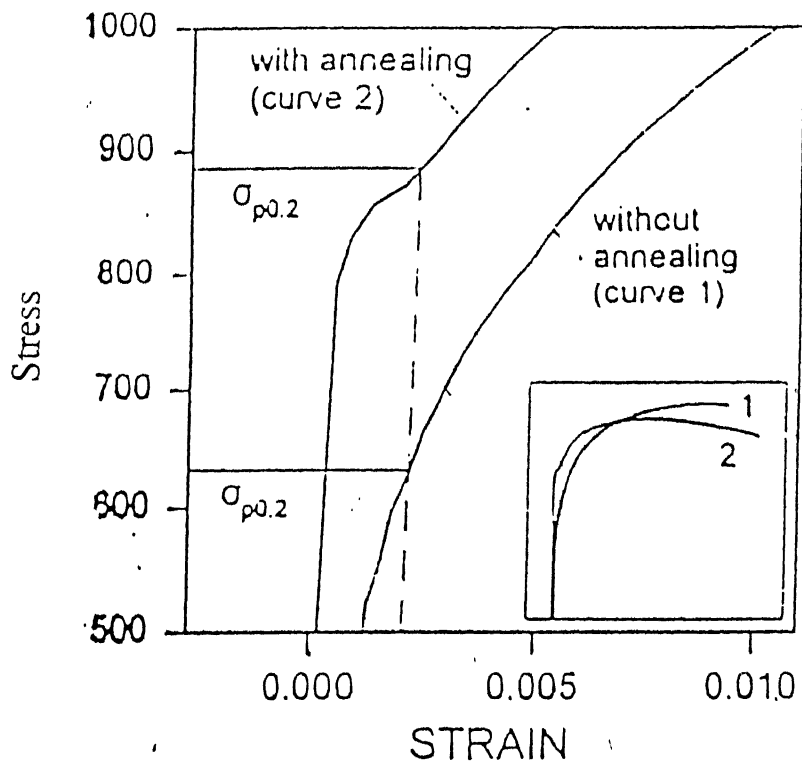


**Figure 1.5 : Influence of an Annealing treatment on the Stress-Strain Curve of Two-Step Cooled steel.**

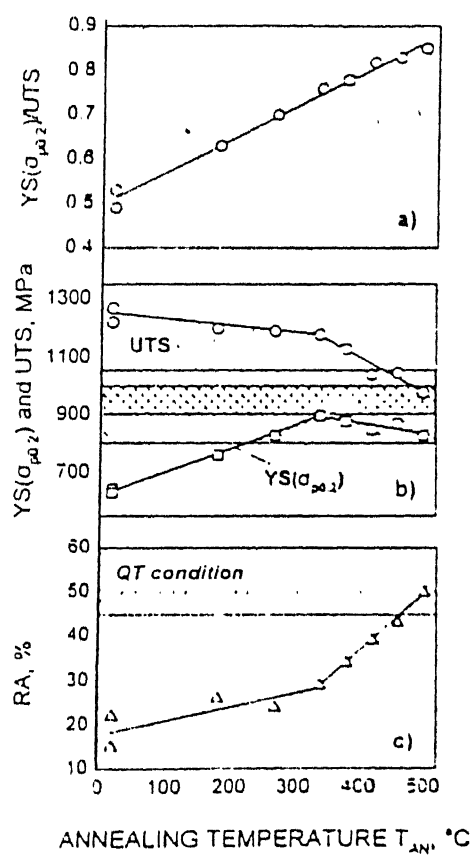


**Figure 1.6:** Mechanical Properties of annealed two-step cooled treatment.

## **1.4**

### **Objectives**

The following objectives were identified for the present investigation.

1. To establish the deformation temperature and the subsequent cooling treatment to be given and the selection of the best thermomechanical route to be adopted.
2. To characterize the microstructures (using qualitative and quantitative analysis) obtained after different thermomechanical treatments, with emphasis on two-step cooling.
3. To correlate the microstructures observed with the final mechanical properties obtained.
4. To study the influence of decrease in deformation temperature in two-step cooling treatment on the microstructure and mechanical properties.
5. To study the effect of annealing on microstructure of thermomechanically treated samples.

## CHAPTER 2

### Literature Review

Thermomechanical processing is the technique designed to improve the mechanical properties of materials by controlling the hot-deformation processes. Such processing saves energy by minimizing or even eliminating heat treatment after the hot deformation, thus increasing the productivity for high-grade steels. It generally demands a change in alloy design, since the necessary mechanical properties are obtained from the alloy composition, and by controlling the heat treatment after deformation [6]. Since the properties are created during the forging and cooling processes, it is very important not only to select the right composition but also to ensure that the appropriate thermomechanical cycle is chosen and then consistently controlled in an industrial environment.

There are certain controlling parameters, which when applied will lead to superior properties [6]. The parameters are:

1. The soaking temperature, which must be high enough to dissolve the microalloying constituent such that it is available to reprecipitate during austenite transformation.
2. The forging temperatures and deformation sequences, with finish forging temperatures particularly important in controlling the austenite grain size and hence the subsequent microstructure. A lower finishing temperature improves the yield to tensile strength ratio and toughness.
3. The cooling rate after forging, with faster cooling rate the transformation temperature lowers down leading to improvement in the strength along with toughness.

The thermomechanical cycle, along with the alloying / microalloying in case of microalloyed steel, influences the microstructure and the mechanical behavior of steel.

So to study the influence of variation in the microstructure on the mechanical properties, it's important that role and significance of every micro-alloying element be known.

## **2.1 Microalloying Elements**

Alloying additives, which can exert a remarkable or specific influence on the properties and microstructure under an addition of less than around 0.10% by weight in steel, are called microalloying elements[7]. The effective and rational utilization of the microalloying elements such as niobium, vanadium, or titanium provides a basis for improvement in both strength and toughness achieved by thermomechanical processing of medium carbon micro alloyed steel. Besides the microalloying elements, substitutional elements (silicon, manganese, magnesium, molybdenum, copper nickel and sulphur) and impurities (phosphorus and sulphur) play a very significant role in obtaining the final properties. Besides strengthening the steel through solid solution hardening, they refine the grains by depressing the austenite to ferrite transformation, ( $\gamma \rightarrow \alpha$ ), temperature and consequently modify the transformed structure. The fundamental behavior of the microalloying elements with respect to solubility, precipitation of carbide or nitride and retardation of austenitic recrystallization, is being discussed in the following section.

### **2.1.1 Solubility Products**

Niobium, vanadium and titanium have different affinities with carbon and nitrogen in austenite ( $\gamma$ ), and this causes the different solubility products of carbide and nitride in respective microalloying element as shown in figure 2.1[7]. In temperature range 1100-1250°C, which is commonly adopted as the billet reheating temperature, titanium nitride (TiN) is the most stable compound and vanadium carbide (VC) the most soluble in austenite ( $\gamma$ ). The stability values for niobium carbide and titanium carbide lies between the stability values of the two compounds (VC and TiN) . Excepting aluminum nitride, which has hexagonal structure, these carbides and nitrides are isomorphous with cubic structures and are soluble in each other, which means that carbide or nitride in steel

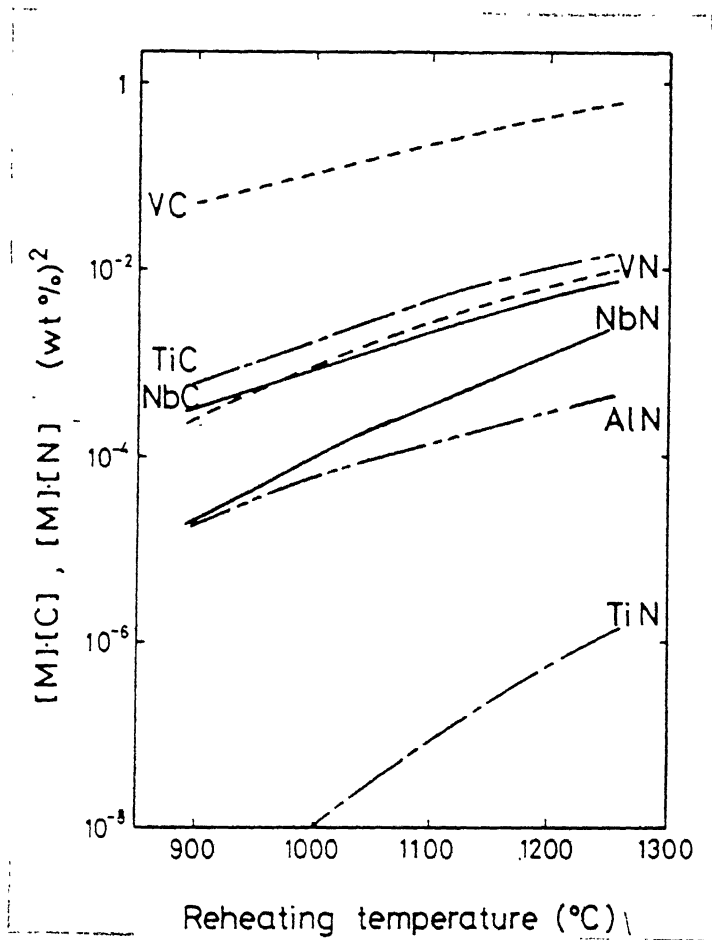


**Figure 2.1:** Solubility Products of Carbides and Nitrides in Austenite.

contains some amount of nitrogen or carbon respectively and are often called carbonitrides[7]. Figure 2.1 shows that all nitrides have lower solubility in austenite ( $\gamma$ ) than the respective carbides and this is also true for ferrite ( $\alpha$ ). In commercial microalloyed steels, vanadium and niobium are precipitated as carbonitrides and VN or NbN are seldom formed. In titanium bearing steel, TiN is formed first and after all the nitrogen is combined as TiN. TiC may subsequently precipitate with increasing titanium content. The undissolved carbides and nitrides at the reheating temperature contribute to refinement of initial austenite grain size. The titanium - bearing steel exhibits an extremely high grain coarsening temperature, above 1250°C. This is because the stable titanium nitride precipitate formed in steel pins the austenitic grain boundaries and inhibits grain boundary motion[7].

### 2.1.2

#### **Retardation of Austenite ( $\gamma$ ) Recrystallisation**

The beneficial effect of controlled deformation, at a high temperature thermomechanical treatment, leads to the retardation of austenitic recrystallisation, due to microalloying elements. The unrecrystallized austenitic grains are elongated and deformation structures are introduced within the grains. This increases the nucleation rate at austenite ( $\gamma$ ) grain boundaries and within austenite ( $\gamma$ ) grains (intragranular nucleation of ferrite). Consequently, this gives rise to very refined transformed microstructure through the transformation from the unrecrystallised austenite. Niobium has the strongest influence amongst all the microalloying elements in this regard[8]. Strain-induced precipitation of carbides and nitrides of niobium takes place in deformed  $\gamma$  primarily causing retardation of recrystallization, while solute niobium may contribute to the suppression of the progress of static recovery in the stage before the start of strain-induced precipitation. The strain induced precipitation of TiC, similar to that of carbides and nitrides of niobium, may occur in titanium bearing steel to cause retardation in recrystallization. But vanadium carbide has high solubility in austenite, as shown by figure. 2.1, so vanadium carbide in vanadium bearing steel tends to maintain vanadium in solution even in the low temperature region of  $\gamma$ ; thus playing no significant role in the retardation of recrystallization.



### 2.1.3

#### Grain Refinement and Precipitation Hardening

The strength and toughness obtained by controlled rolling in microalloyed steel largely depends on grain refinement and precipitation hardening. The stability and slow growth rate of TiN renders it as an effective grain growth inhibitor. The combined effect of TiN and MnS suppresses extreme coarsening of austenite grains [4]. Nb also helps in grain refinement by inhibiting recrystallisation of austenite. In the non-recrystallized  $\gamma$  grains deformation bands are present. So ferrite ( $\alpha$ ) nucleates on deformation bands and their twin bands as well as on austenite ( $\gamma$ ) grain boundaries, having an increased surface area for  $\gamma \rightarrow \alpha$  transformation and hence finer microstructure is obtained. The precipitation hardening by microalloying elements can enhance the hardenability of steel and can significantly affect the transformation behavior. It is known that presence of microalloying elements can alter transformation behavior and the resultant microstructure can shift from  $\alpha$ -pearlite to  $\alpha$ -bainite as will be explained in the next section.

## 2.2

### Microstructures in Steel

High-temperature austenite can transform into the low-temperature phases, ferrite and carbide, during cooling in very different ways, from which the complexity of steel microstructure results [9]. The particular reactions depend sensitively on the chemical composition of the steel, on the austenite state (grain size, degree of homogeneity) and in particular on the cooling rate. This section gives an overview of the microstructure and constituents, which are formed in steels during cooling from austenite temperature range to room temperature.

#### 2.2.1

##### Cementite ( $\text{Fe}_3\text{C}$ )

When steels are slowly cooled from the temperature where austenite is stable, depending on carbon and alloy content, cementite forms at temperatures along the  $A_{cm}$ . The growth

of cementite requires diffusion of carbon from the austenite ( $\gamma$ ) to the cementite and a rearrangement of the iron atoms from the fcc structure, to that of the iron atoms in the orthorhombic structure of cementite[10]. Cementite nucleates at austenite ( $\gamma$ ) grain boundaries that are sites of higher energy and have greater atomic disorder than the grain interiors. The growth of cementite allotriomorphs is accomplished by a ledge-type mechanism that proceeds at  $\text{Fe}_3\text{C}$ -austenite interface consisting of flat faces joined by steps or ledges[11]. The flat faces are coherent or semi-coherent and have low mobility while the ledges are interfaces with higher disorder, which enhances atomic transfer.  $\text{Fe}_3\text{C}$  growth is rapid when only carbon diffusion and iron atom rearrangement is required. If substantial amount of carbide forming elements, such as chromium, have to partition from  $\gamma$  to the growing  $\text{Fe}_3\text{C}$ , the growth rate becomes very sluggish[12]. Since the carbon content of even high carbon steels is not sufficient to produce large volume fraction of  $\text{Fe}_3\text{C}$ , the cementite networks are always relatively thin.

### 2.2.2

#### Ferrite ( $\alpha$ )

In low and medium carbon steels ferrite ( $\alpha$ ) allotriomorphs first begins to form, at temperatures along the  $A_3$ , when austenite ( $\gamma$ ) is cooled [10]. With increasing carbon content in steel ferrite ( $\alpha$ ) starts forming at lower and lower temperatures. Ferrite allotriomorphs nucleate at austenite grain boundaries and grow into the austenite grain interiors [11-13]. Evidence shows that growth occurs at ledges with high interfacial mobility. In any given steel, as the ferrite allotriomorphs grow, carbon is rejected into the surrounding austenite because of its very low solubility in the bcc structure of ferrite. As a result, the austenite becomes increasingly enriched in carbon. When the carbon content of the austenite reaches about 0.8%, the eutectoid transformation of austenite to pearlite, which is a mixture of ferrite and cementite of lamellar form, occurs as described in the next section.

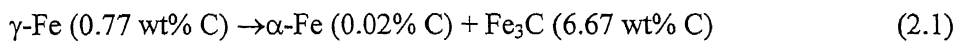
Theoretically, substitutional alloying elements should partition between ferrite and austenite according to the requirements of thermodynamic equilibrium. However, under conditions of high undercooling or high supersaturation in steels with alloying elements / microalloying elements the  $\gamma \rightarrow \alpha$  transformation may take place with only the required

carbon rejection from the ferrite and no change occurs in the substitutional alloying element content of the two phases. Under conditions of low undercooling or low supersaturation, substitutional alloying elements attempt to partition between the ferrite and austenite in order to maintain local equilibrium at the interface between the two phases [13-14]. Thus ferrite stabilizing substitutional elements diffuse from  $\gamma$  to  $\alpha$  and austenite-stabilizing elements are rejected from  $\alpha$  into  $\gamma$ . The growth kinetics of the ferrite then becomes dependent on the diffusion of substitutional elements and is slowed considerably relative to growth controlled by carbon diffusion. When ferrite growth rates are retarded sufficiently, rapid cooling or quenching of austenite causes its transformation to martensite or bainite, as will be described later.

The ferrite grain boundary allotriomorphs, which grow uniformly into the austenite grain interiors, produce the equiaxed ferrite grain morphology. Another morphology of ferrite that may form in low alloy steel consists of plate or lath shaped crystals of ferrite. These elongated crystals are referred to as Widmanstätten ferrite and tend to form under conditions of substantial undercooling for austenite to ferrite transformation. The lath shape and the surface relief associated with the formation of the laths indicates that shear may contribute to Widmanstätten ferrite formation, but other evidence shows that the interfaces of the ferrite laths contain structure which apparently are associated with diffusion-controlled growth [14].

### 2.2.3 Pearlite

Pearlite can be distinguished from other transformations by its kinetics as well as by its microstructure. There is a certain temperature range in which the eutectoid reaction (given by equation 2.1) that results in the pearlitic structure, takes place [10].



The mixture of ferrite and cementite, which forms as a result of the eutectoid transformation in steels, has a unique lamellar morphology and is referred to as pearlite. Pearlite nucleates in the same way as proeutectoid ferrite or cementite, preferentially at

austenitic grain boundaries or at the interfaces of austenite with one of the proeutectoid precipitates. The nucleation of a pearlite colony requires the simultaneous nucleation of two phases in order to establish the lamellar morphology of pearlite [15]. In hypoeutectoid and hypereutectoid steels, steels of lower and higher carbon content than the eutectoid composition respectively, the pearlite colonies are nucleated by the proeutectoid phases [10]. In eutectoid steel, nucleation of pearlite colonies may occur by multiple nucleations of parallel ferrite and cementite lamellae [16]. Ferrite and cementite are formed during nucleation in such a way that the interface and elastic volume energies are minimized by certain crystallographic relationship, as given below between the cementite and ferrite lamellae within a pearlite nodule.

**Pitsch / Petch relationship** (2.1)

$$\begin{aligned}(001)_c // (5\bar{2}1)_\alpha \\ (010)_c \text{ } 2\text{-}3^\circ \text{ from } [11\bar{3}]_\alpha \\ (100)_c \text{ } 2\text{-}3^\circ \text{ from } [13\bar{3}]_\alpha\end{aligned}$$

**Bagaryatski relationship** (2.2)

$$\begin{aligned}(100)_c // (0\bar{1}\bar{1})_\alpha \\ (010)_c // (1\bar{1}\bar{1})_\alpha \\ (001)_c // (211)_\alpha\end{aligned}$$

The transformation produces not only distinct crystallographic relationships between the two new phases but also relationship between these phases and the former austenite. During the growth of pearlite nucleus, due to increased or decreased carbon concentration in the austenite matrix at the ferrite or cementite side, cementite or ferrite is nucleated again. Accordingly the pearlite colony widens by alternating formation of ferrite and cementite whereas perpendicular to this process both phases grow simultaneously in a coupled manner. The characteristic feature of the growth of pearlite is the absence of long distance diffusion of carbon in the austenite. Instead carbon is redistributed by short-range diffusion in such a way that in neighboring regions, with increased or decreased carbon concentrations; cementite or ferrite is formed, respectively. The

formation of pearlite is influenced by most of the substitutional elements, and is usually retarded. The alloying elements segregate at the grain boundaries and suppress the nucleation of pearlite. Subsequently increased fractions of bainite/martensite are formed [10].

#### **2.2.4 Martensite**

Austenite transformation to ferrite, cementite or pearlite, as described above, occurs by carbon, iron and substitutional atom diffusion. If austenite is cooled very rapidly or if steel is so alloyed so as to significantly slow atom transfer, there is insufficient time for diffusion and thus austenite transforms to martensite. Martensite is a phase, which forms by athermal diffusionless displacive mechanism. The martensite transformation produces a homogeneous displacement or shape change, which produces a characteristic, tilted surface relief. Martensite forms on specific crystal planes of the parent austenite, referred to as habit planes, that is function of steel composition and the temperature range over which the martensite forms. In order to accommodate the displacement associated with the formation of a martensite crystal, the parent austenite also deforms. The existence of a lattice correspondence is the hallmark of a martensitic or shear transformation. This means that geometrically each atom in the parent phase can be related to corresponding atom in the product phase, but the corresponding vectors in each lattice are not equal and angular relationships between planes are not preserved.

Martensite is modeled by a crystallographic theory, which assumes that the shape change is accomplished by a homogeneous plane strain, which leaves the habit plane unrotated and undistorted [17-20]. Two deformations, lattice deformation and lattice invariant deformation, are required to accomplish the shape change as shown in figure 2.2. Lattice deformation leads to crystal structure change from austenite to martensite (Bain strain). Bain strain involves the smallest atomic displacements. This is the homogeneous shape deformation which, when combined with a fine scale inhomogeneous deformation (lattice invariant), led to an undistorted interface. The inhomogeneous lattice invariant deformation was assumed to result from dislocation movement, which could be in the form of deformation by slip or twinning. Figure 2.3

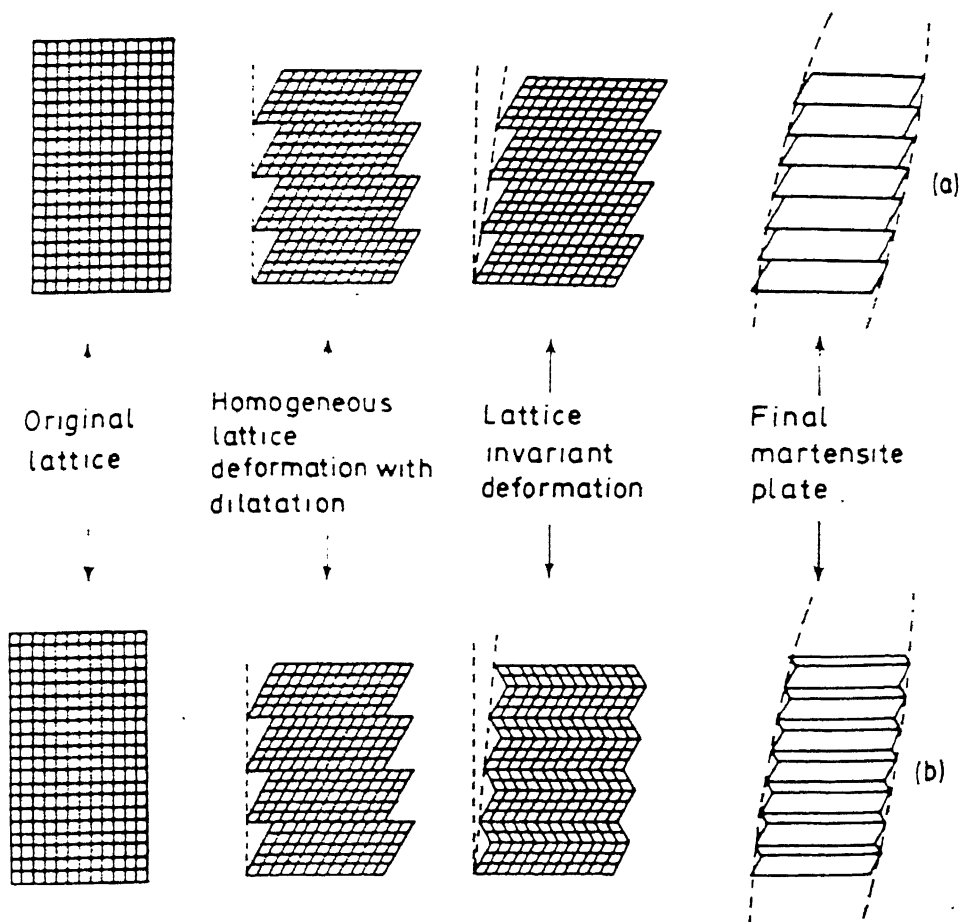


**Figure 2.2:** Schematic Diagram Illustrating the Combined Effect of Lattice Deformation and Lattice Invariant Deformation

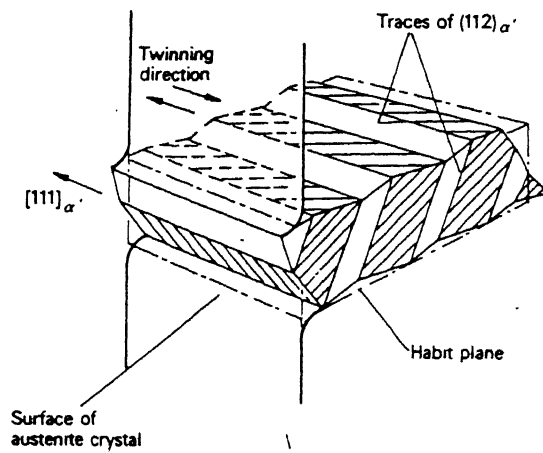
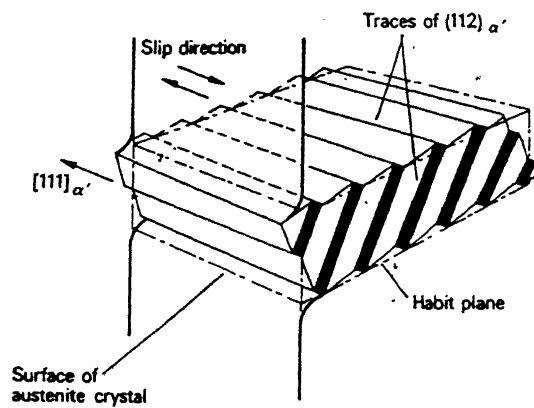


**Figure 2.3** Schematic Diagram Illustrating Two Types of Lattice Deformation: Slip and Twin

shows schematically the two types of lattice invariant deformation occurring in a martensite plate. Both these processes are capable of accommodating the misfit, which would otherwise occur at the austenite / martensite interface as a result of the deformation that causes both the macroscopic change, and the transformation of the original lattice from face-centered cubic to body centered tetragonal.

There exists a certain orientation change that occurs when a martensite plate is formed inside an austenite grain [21]. While the observed relationships can change with composition, in all ferrous systems the closest packed planes are approximately parallel.  $\{111\}_\gamma$  is parallel to  $\{110\}_\alpha$ . The two main relationships (equations 2.3 and 2.4) are described by the parallelism of different lattice directions, amounting to several degrees difference in orientation [21].

$$\textbf{Kurdjumov-Sachs} \quad (2.3)$$

$$\langle 011 \rangle_\gamma // \langle 111 \rangle_{\alpha'}$$

$$\textbf{Nishiyama / Greninger \& Troiano} \quad (2.4)$$

$$\langle 112 \rangle_\gamma // \langle 011 \rangle_\alpha$$

Substantial thermodynamic driving force or undercooling of the parent austenite is required to initiate lattice shearing to martensite. The temperature at which the transformation starts is defined as the  $M_s$  temperature and is a function of carbon and substitutional alloying elements[22].

$$M_s(^{\circ}\text{C}) = 539 - 423C - 30.4 \text{ Mn} - 12.1\text{Cr} - 17.7\text{Ni} - 7.5 \text{ Mo} \quad (2.5)$$

In the equation 2.2 the elemental designations refer to the amount in wt%. This equation shows the powerful effect of interstitial carbon in suppressing  $M_s$  and all of the substitutional elements also lower  $M_s$  but to a lesser degree.

Two types of martensitic microstructure and morphologies, lath and plate, develop in steels. The two morphologies differ with respect to their fine structure, habit planes and the arrangement of the martensitic units within a transformed structure[23-24].

1. Lath martensite forms in low and medium carbon steels with relatively high  $M_s$  temperature and it is believed to be broad shaped or lath-like, hence the name of this morphology. The martensite laths align themselves parallel to one another in



arrays referred to as packets. The laths are quite fine and are below the resolution of the light microscopy. The fine structure within lath martensite consists of high densities of tangled dislocations, consistent with the dislocation mode of plastic deformation to accomplish the lattice invariant deformation.

2. Plate martensite forms in high carbon steels with low  $M_s$  temperatures [25]. The units of this kind of martensite are plate shaped and their cross-sections on polished-etched surfaces produce the characteristic needle-like or acicular shapes. Adjacent plates tend to form at angles to each other, in contrast to the parallel unit alignment in lath martensites. Therefore plate martensite microstructure appears to be more irregular than those of lath martensite. The fine structure of plate martensite is often composed of very fine transformation twins or screw dislocation arrays consistent with plastic deformation mode characteristic of b.c.c deformed at low temperature.

### **2.2.5**

#### **Bainite**

Bainite is a two-phase microstructure, which is formed by austenite transformation between the temperature ranges at which pearlite and martensite form[26]. Similar to pearlite, the classical form of bainite consists of ferrite and cementite. However the mechanisms of transformation and the morphologies of the resultant ferrite and carbide structures of pearlite and bainite differ significantly (figure 2.4). The diffusion of carbon atoms and the short-range diffusional transfer of iron/ substitutional atoms form pearlite across the austenite-pearlite interfaces, and this defines the spherical colonies of pearlite. Bainite forms at lower temperatures than pearlite, where even short-range iron/substitutional atom transfer is suppressed. As a result, bainitic ferrite is nucleated by a cooperative iron atom shear mechanism and the morphology of the ferrite takes on the plate or lath appearance of martensite rather than the spherical or equiaxed morphology of pearlite and proeutectoid ferrite. Carbon is, however, able to diffuse and therefore various temperature-dependent arrays of cementite particles are associated with bainite. The cementite particles are not continuous as they are in pearlite, leading to a

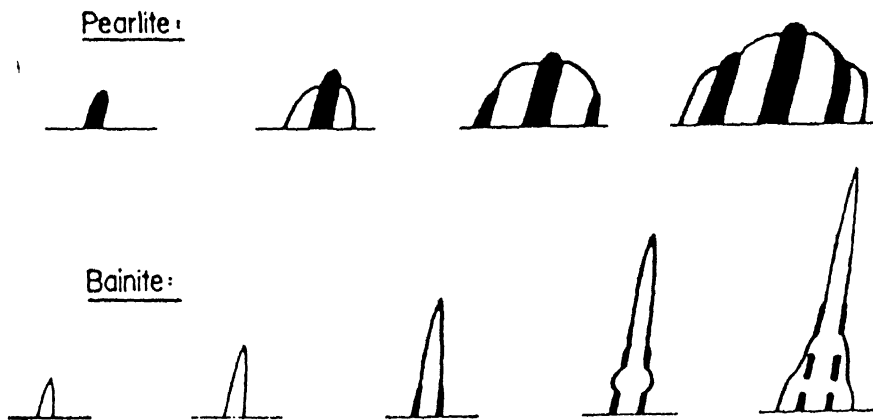


**Figure 2.4** Schematic Diagram Illustrating the Difference in the Shape of Pearlite and Bainite

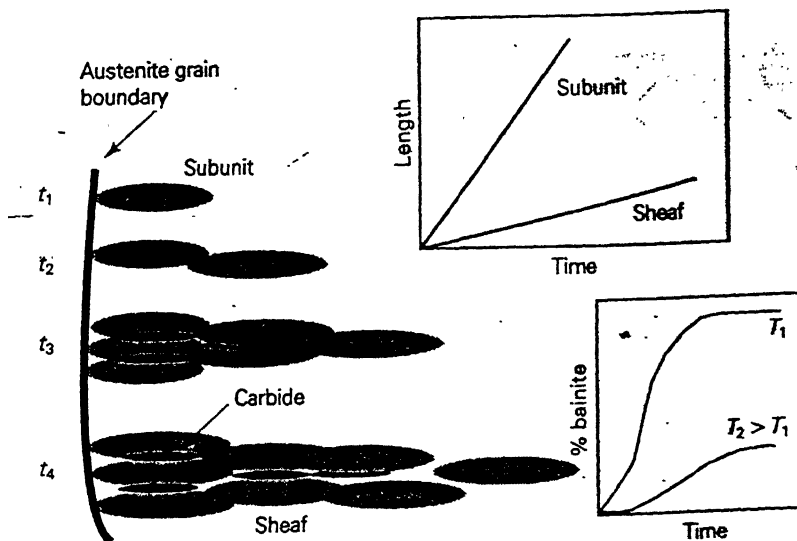


**Figure 2.5** Schematic Diagram Illustrating the Microstructural Factors Relevant in the Kinetic Description of Bainite.

.metallographic definition of bainite as a structure consisting of a non-lamellar array of ferrite and cementite [23-24].

The bainite transformation remains the least understood of all the decomposition reactions of austenite. The complexity of its formation mechanism, kinetics and apparent diversity in the microstructural appearance will be discussed. The rate of the bainite reaction is divided into a number of distinct events as shown by figure 2.5 [27-29]. A sub-unit nucleates at the austenite grain boundary and lengthens at a certain rate before its growth is stifled by plastic deformation within the austenite. New sub-units then nucleate at its tip, and the sheaf structure develops as the process continues. The overall lengthening rate of a sheaf is therefore smaller than that of an individual sub-unit because there is an interval between the formations of successive sub-units. Carbide precipitation events also influence the kinetics, primarily by removing carbon either from the residual austenite or from the supersaturated ferrite. Two different morphologies of bainite exist, upper bainite and lower bainite [27-28].

**Upper bainite (temperature range 550-400°C):** The microstructure of upper bainite consists of fine plates of ferrite, each of which is about 0.2  $\mu\text{m}$  thick and about 10  $\mu\text{m}$  long [29]. The bainite grows in form of sheaves, which are clusters of connected platelets, which grow in parallel formations and are of identical crystallographic orientation. The carbon diffusion field associated with each platelet to large extent, controls the spacing between the platelets; therefore the increase in platelet thickness is restricted by the diffusion fields and by the presence of adjacent platelets. The individual plates in a sheaf are often called the 'sub- units' of bainite and are usually separated by cementite particles.

The growth of each plate is accompanied by a change in the shape of the transformed region, a change that has been described as an invariant plain strain with a large shear component [32]. The growth of each plate is accompanied by an invariant-plane strain with a large shear component. The need to minimize strain energy demands a thin plate, but this also leads to minimization of the volume of transformation per plate. Therefore a plate will tend to adopt the largest aspect ratio consistent with the available free energy change driving the transformation. A further complication is that the upper bainite transformation occurs at high temperature where the austenite is mechanically weak. The

shape deformation therefore causes plastic deformation and the resulting dislocation debris eventually blocks the transformation interface, which loses coherency. Hence the platelets of bainite are arrested in their growth even when their size is much smaller than the austenite grain size. The shape change associated, implies that the mechanism of the growth of bainitic ferrite is displacive. It is the minimization of the strain energy associated with the displacements that ensures that the bainite grows in the form of thin plates. A coordinated movement of atoms generates the crystal structure of bainite. There exists an orientation relationship between the austenite and bainite and bainite forms on particular crystallographic planes

Upper bainite forms in two distinct stages, the first involving the formation of bainitic ferrite which has a very low solubility for carbon. The growth of ferrite therefore enriches the remaining austenite in carbon. Eventually, cementite precipitates from the residual austenite layers in between the ferrite sub-units[29]. The amount of cementite depends on the carbon concentration of the alloy [32]. High concentrations lead to microstructures in which the ferrite platelets are separated by continuous layers of cementite. Small, discrete particles of cementite forms when the alloy carbon concentration is low. The cementite particles have a ‘Pitsch’ orientation relationship (equation 2.6) with the austenite from which they precipitate[28-29]:

**Pitsch Relationship:** (2.6)

$$(001)_{\text{Fe}_3\text{C}} // (\bar{2}25)_{\gamma}$$

$$[100]_{\text{Fe}_3\text{C}} // [\bar{5}\bar{5}4]_{\gamma}$$

$$[010]_{\text{Fe}_3\text{C}} // [\bar{1}\bar{1}0]_{\gamma}$$

**Lower bainite (temperature range 400-250°C):** Lower bainite has a microstructure and crystallographic features which are very similar to those of upper bainite. The major distinction is that cementite precipitates inside the plates of ferrite. The cementite particles in lower bainite exhibit only one variant of the orientation relationship, such that they form parallel arrays at about 60° to the axis of the bainite plate. This feature of the precipitate suggested that it has not precipitated within plates saturated with respect to carbon, but it has nucleated at the  $\gamma/\alpha$  interface and grown as the interface had moved forward [33]. Thus the lower bainite reaction is basically an interface-controlled process

leading to cementite precipitation, which then decreases the carbon content of the austenite and enhances the driving force for further transformation.

The carbides in lower bainite are extremely fine; just a few nanometers thick and about 500 nm long [29]. Because they precipitate within the ferrite, a smaller amount of carbon is partitioned into the residual austenite. In contrast to upper bainite, the individual ferrite plates in lower bainite are more regular and these ferrite plates are very thin because of the smaller diffusivity of carbon in austenite at the lower temperature. It has been found that ferrite plates thicken by the repeated precipitation of carbides at the advancing interface[34]. The dislocation content of ferrite was found to be high relative to upper bainite's ferrite.

The transformation begins with the formation of the usual small sub-units of lower bainite at an austenite grain boundary but the sub-units then coalesce to form a single larger plate. The subunits can combine and grow if there is sufficient driving force to sustain the larger amount of strain energy associated with a thicker plate and there is nothing to stifle the lengthening of the sub-units [35]. It implies that coalescence can only occur in the early stages of transformation, when the growth cannot be hindered either by hard impingement with other regions of bainite, or by soft impingement processes. Moreover, at lower temperature shape deformation accompanying the growth of bainite is more elastically accommodated since the yield strength of all phases increases as the temperature is reduced. Thus, the sub-units grow to longer lengths.

Similar coalescence effects were not found for upper bainite, presumably because of lower chemical driving force available at higher transformation temperature [36-38]. A greater degree of plastic deformation occurs due to reduced yield strength and the carbon tends to partition more rapidly from supersaturated ferrite at higher temperature. Consequently, the distribution of plates was observed to be much more uniform [38].

The classical nomenclature of upper and lower bainite is given by difference in carbide distribution, intralath and interlath, respectively. But recently it has been studied that cementite precipitation cannot be the index for the classification and bainite should be classified by ferrite morphology, viz. lathlike or platelike. The classification of bainite by the ferrite morphology of being either lathlike or platelike would be adopted for the present investigation [31].

The bainite reaction has several of the recognized features of a nucleation and growth process. It takes place isothermally, starting with an incubation period during which no transformation is detected, followed by an increasing rate of transformation to a maximum and then a gradual slowing down. It is clear that the extent of transformation is a sensitive function of temperature and this is totally characteristic to the incomplete reaction phenomenon [39-41].

**The transition from upper to lower bainite:** As the isothermal transformation temperature is reduced below  $B_s$ , bainitic transformation start temperature, lower bainite is obtained in which the carbides precipitate in the ferrite with a correspondingly reduced amount of precipitation from the austenite between the ferrite [30]. This transition from upper to lower bainite can be explained in terms of the rapid tempering processes that occur after the growth of a supersaturated plate of bainite as shown in figure 2.6. Excess carbon tends to partition into the residual austenite by diffusion, but the supersaturation may also be reduced by precipitation within the ferrite. At elevated temperatures the diffusion is so rapid that there is no opportunity to precipitate carbides in the ferrite, giving rise to an upper bainitic microstructure. Cementite eventually precipitates from the carbon-enriched residual austenite. As the transformation temperature is reduced and the time for decarburization increases, some of the carbon has an opportunity to precipitate as fine carbides in the ferrite, whereas the remainder partitions into the austenite, to precipitate as inter-plate carbides and lower bainite is obtained.

Carbon has a large effect on the range of temperature over which upper and lower bainite form. The  $B_s$  temperature is depressed by many alloying elements but carbon has the greatest influence, as indicated by the empirical equation 2.7 [29-30].

$$B_s (^{\circ}\text{C}) = 830 - 270(\%C) - 90(\%Mn) - 37(\%Ni) - 70(\%Cr) - 83(\%Mo) \quad (2.7)$$

The carbon concentration also influences the temperature of transition from upper to lower bainite as shown in figure 2.7. This transition temperature can be defined as the temperature at which diffusivity of carbon becomes too slow to allow diffusion away from the  $\gamma/\alpha$  interface. Hence in steels containing high concentrations of carbon, only lower bainite is obtained. The large amount of carbon that is trapped in the ferrite by transformation cannot diffuse fast enough into austenite so that precipitation from ferrite

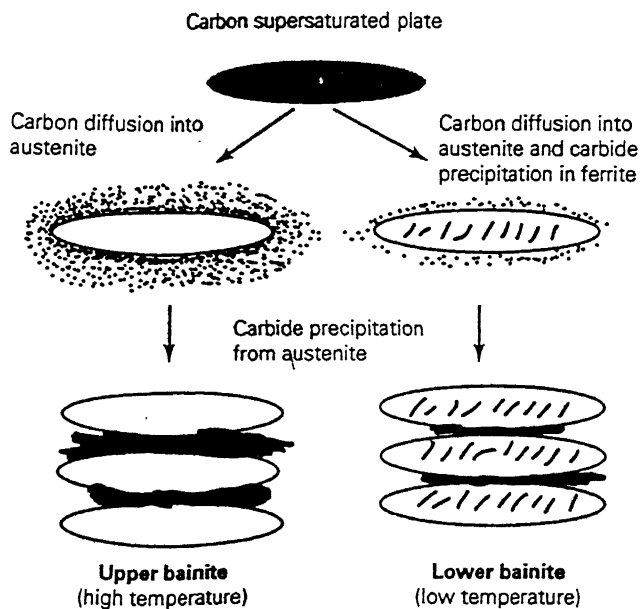
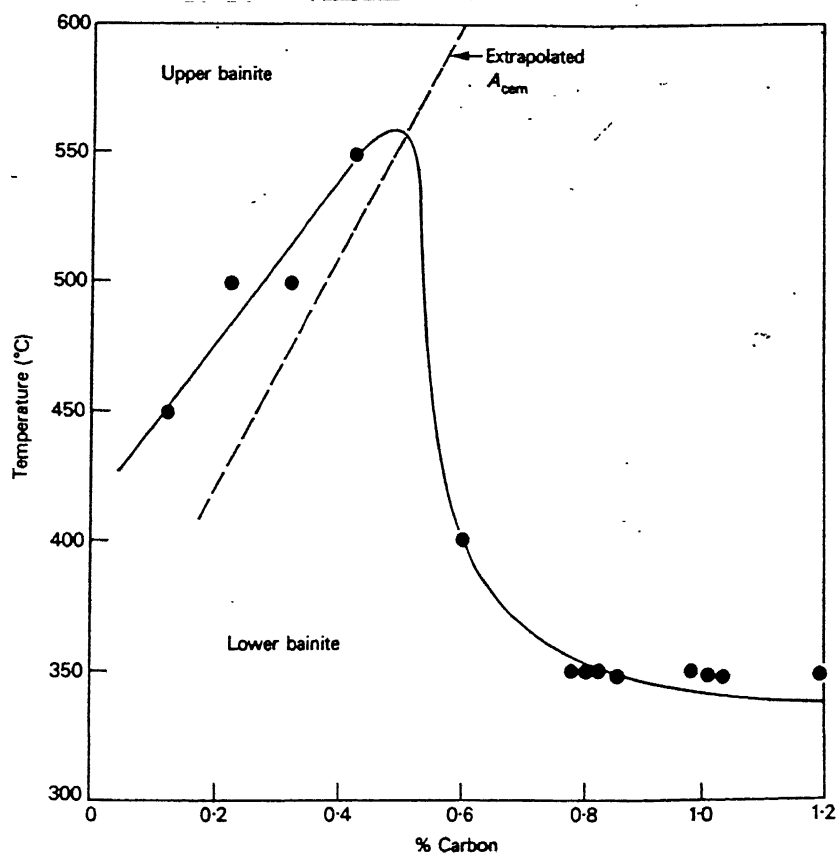


**Figure 2.6** Effect of Carbon Content on the Temperature for Transition from Upper to Lower Bainite.



is unavoidable. Conversely, in low carbon steels, the time for decarburization is so small that upper bainite is only obtained.

**Advantages of bainitic steels:** The bainitic steels are increasingly being used because the strength achieved is very high. Yield strength in the range 450-900 MPa can be attained which is much above that of ferrite-pearlite structure [30]. For a constant cooling rate, the strength of steel can be increased significantly by lowering the  $B_s$  temperature, which can be achieved by the addition of carbon and other alloying elements. The linear empirical relationship between the tensile strength and composition has been indicated in equation 2.8 [30].

$$\text{TS (MPa)} = 15.4 [16 + 125 (\% \text{ C}) + 15 (\% \text{ Mn} + \% \text{ Cr}) + 12 (\% \text{ Mo}) + 6 (\% \text{ W}) + 8 (\% \text{ Ni}) + 4 (\% \text{ Cu}) + 25 (\% \text{ V} + \% \text{ Ti})] \quad (2.8)$$

The operating strengthening mechanisms in bainite steel are

1. A fine bainitic ferrite grain size due to low transformation temperature that gives a Hall- Petch relationship with yield stress;
2. Increased dislocation density due to increased transformation strains associated with the decrease in transformation temperature and the formation of dense carbides;
3. Increased carbide dispersion strengthening with the increasing carbon content and decreasing transformation temperature, the dispersion being denoted by the number of carbide particles per unit planar surface area;
4. Increased interstitial solid solution hardening of bainitic ferrite with decreasing transformation temperature;
5. Strengthening by interaction of solute atoms with dislocations.

Bainitic steels also show significant toughness. Lower bainite has a lower- impact temperature (ITT) and upper bainite has a higher ITT; this is mainly because of much greater transition temperature range in the lower bainite than in the upper bainite[30]. Lower bainite exhibits a finer ferrite plate size and a higher dislocation density than upper bainite. The fine carbides within ferrite plates impede the propagation of cleavage cracks because of their different orientations and high- angle ferrite boundaries; therefore



fracture toughness is raised. In upper bainite, where propagation of cleavage cracks by coarse carbides easily occurs at the low - angle lath boundaries across the high - angle prior austenite boundary, ITT is raised and lower toughness value is obtained.

So with bainitic steels relatively high strength associated with improved ductility can be obtained and that has extensively increased their industrial use.

## CHAPTER 3

### Experimental Procedure

In this chapter, the experimental techniques used are discussed in detail. The initial part of the chapter deals with the details of the starting material used in the present work and the thermomechanical treatment performed on it. This is followed by discussion of various characterization methods adopted, namely the quantitative microscopic measurements as well as mechanical testing.

#### 3.1 Starting Material

The starting material used in the present investigation is a microalloyed medium carbon steel and was produced at Tata Iron and Steel Company, Jamshedpur, India. The microalloyed medium carbon forging steel was received in the form of forged bars of 30mm diameter. The chemical composition of the material found by the use of spectrometer is given in table 3.1.

**Table 3.1:** Chemical composition of 38MnSiVS6

| Material  | C    | Si   | Mn  | P     | S    | V    | N     | Cr   | Fe      |
|-----------|------|------|-----|-------|------|------|-------|------|---------|
| 38MnSiVS6 | 0.38 | 0.68 | 1.5 | 0.022 | 0.06 | 0.11 | 0.006 | 0.18 | balance |

#### 3.2 Thermomechanical Processing

The thermomechanical treatment involved forging over a temperature range 1100°C to 800°C and was followed by two-step cooling. The forging was done in Field Gun Factory, Kanpur, using a 500 tonnes Hydro-Pneumatic hammer. Some of the samples were quenched in water after being forged and tempered. The flowchart shown in figure 3.1 shows the thermomechanical route adopted in the present investigation.

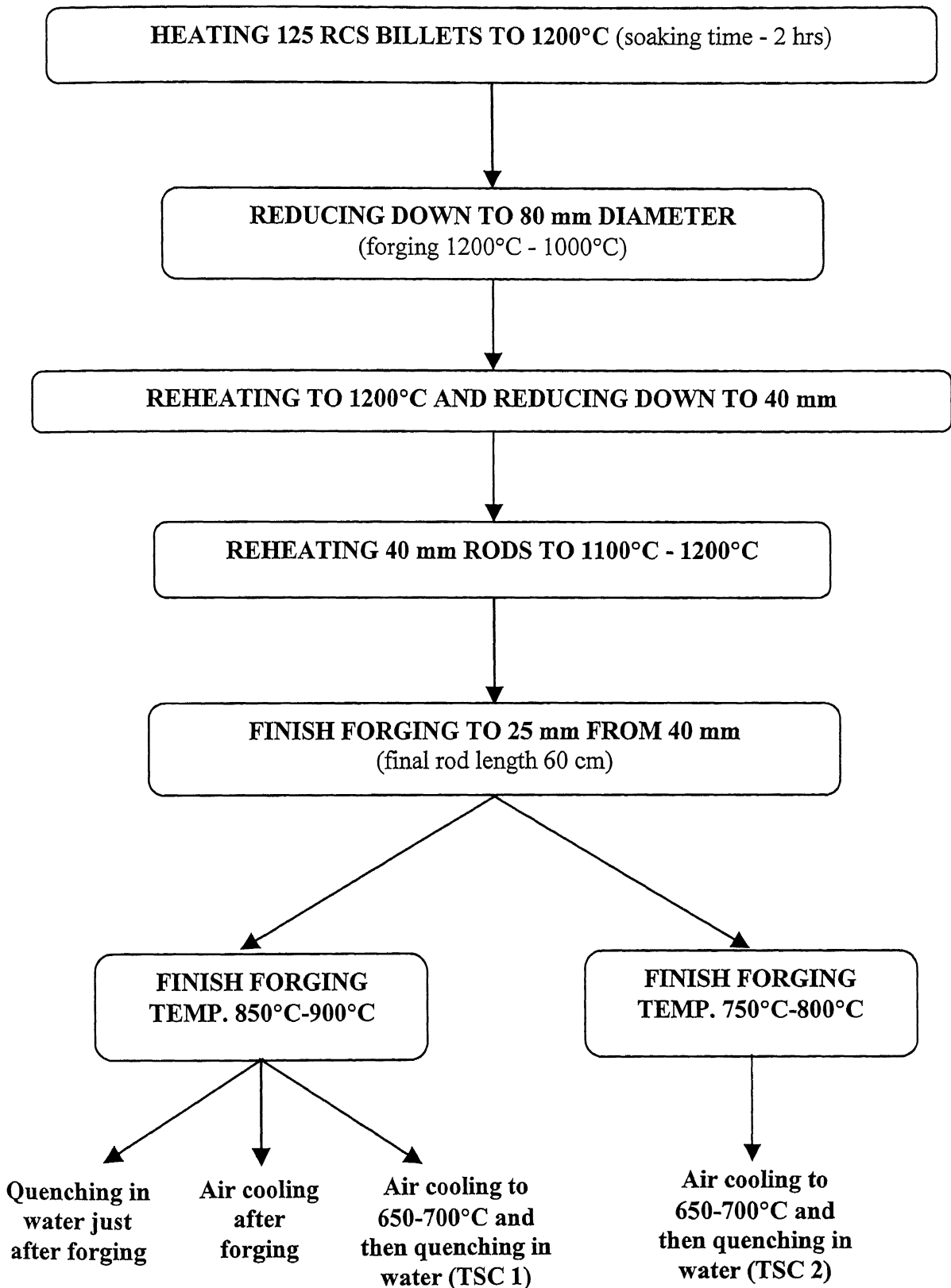


**Figure 3.1:** Thermomechanical treatment given to 38MnSiVS6

The austenisation temperature was 1200°C, at which the dissolution of the microalloying carbides were found to be convenient. The billets were forged to the final dimension in steps as shown in the flowchart. The final forging was done to keep the final diameter of the rods as 25 mm.

In order to study the affect of deformation temperature and cooling rate on the final structure and properties obtained, varied thermomechanical treatments were given to the same material. Few samples were quenched in water immediately after forging at temperature 850-900°C, to obtain martensitic structure and a few were cooled in air after forging in the same temperature range to study the effect of continuous cooling treatment. The last set of samples were given two step cooling treatment (TSC). After finish forging at 850-900°C, they were allowed to air cool to 650-700°C (slow cooling step) and after that samples were quenched in water (fast cooling step). This grade of thermomechanically treated material will be subsequently referred to as TSC1. To verify the importance of lowering of deformation temperature, few samples were finish forged at comparatively lower temperature (750-800°C). After forging the samples were air cooled to 650-700°C and then quenched in water. This treated grade will be hereafter referred to as TSC2.

The TSC1 and TSC2 samples were annealed to study the importance of annealing treatment on the mechanical properties. The annealing treatment was carried out at different temperatures and for different time intervals for optimization of annealing cycle. The annealing temperatures chosen for study were 400°C, 425°C, 475°C and 500°C. The time interval for annealing was kept as 1hr, 1.5hrs, 2hrs and 2.5hrs. The time-temperature relation with respect to microstructure was obtained and the optimum mechanical properties were derived by various characterization methods adopted. In the following section the various techniques applied for characterization of the samples are discussed in detail.

### **3.3**

#### **Quantitative Microscopy**

This section includes the procedure involved in the preparation of the samples, which were to be observed under the microscope. The sample preparation is followed by details

of the procedure adopted for micro structural observation and the stereological study performed on the sample for the purpose of characterization.

### **3.3.1**

#### **Sample Preparation**

The preparation of the samples is an integral part of the microscopic study. The samples were cut from the forged rod by using abrasive wheel cutter. The cut samples were ground using a belt grinder followed by polishing of ground samples on emery sheet of various grades (1 to 4 grades). The paper-polished samples were then wheel polished. Alumina powder of 1 $\mu$ m was used for coarse wheel polishing and 0.3  $\mu$ m was used for fine wheel polishing. The mirror-like polished samples were etched using 3% Nital solution. The prepared samples were used for the microstructural study by making use of optical and scanning microscope.

### **3.3.2**

#### **Optical Microscopy**

Optical microscope was used for low magnification microstructural study. The prepared samples were observed under the microscope at low magnifications of 200X 500X and 1000X. Low magnification was used because it was observed that at this magnification, the morphology of bainite could be conveniently studied. The unannealed TSC1 and TSC2 rods were characterized with respect to microstructure by using optical microscope. The samples were cut along the length of the rods, which were approximately 60 cms long, at a regular distance of 4cms. An effort was also made to measure the volume fraction of the various phases present in the sample, taken from the length of the rod. The optical microscope was extensively used but it was felt that low magnification was not suitable for the detailed study of the constituent phase hence scanning electron microscope was also used.

### 3.3.3 Scanning Electron Microscopy

Most of the microstructural study with regards to the individual phase features was done with scanning electron microscope (JEOL-JSM 840A). The polished samples were seen under the scanning electron microscope, operated at 15KV, using secondary electron radiation (SE mode). Various micrographs were taken at 10,000X, 7500X, 5000X and 2500X using the camera attached to SEM. These micrographs were subsequently used for microstructural study and stereographic measurements. The advantage of using highly magnified micrographs is that the details of individual phases, which include phase morphology, size, surface characteristics and various other features, are clearly visible at the high magnifications used. The extensive characterization of TSC1 and TSC2 rods became feasible due to the high magnification study. During the course of work SEM was out of order for a short duration during which electron probe micro-analyzer (JEOL JXA-6300MXA) was used as an alternative for taking microstructure's photographs.

### 3.4 Stereological Measurements

Stereology is a body of mathematical methods, relating 3-dimensional parameters to 2-dimensional measurements obtainable on sections of the structure. Using stereology its possible to give quantitative interpretation of 2-dimensional observations in terms of 3-dimensional parameters. In this study, some mathematical relations have been used and the measurements made on micrographs have been related to the sample. Volume fraction ( $V_v$ ) of the various phases present the samples were measured using a rectangular grid of 100 points. In some samples the ferrite fraction was very less and the ferrite grain size was also very small so point count method was found to be a more convenient method for  $V_v$  measurement. The volume fraction of the phases was measured, either by point count or rectangular grid method, directly using a screen attached to the optical microscope. The mathematical relation used for the measurement of volume fraction is shown in equation 3.1.

$$V_v = P_p \quad (3.1)$$

Where  $P_p$  is the fraction of points lying in the phase under consideration.

For the measurement of volume fraction of bainite constituents, ferrite and cementite, SEM micrographs were used and rectangular grid with 100 points was used for it. For the measurement of surface area per unit volume ( $S_V$ ) of bainite the mathematical relation, given in equation 3.2, was used.

$$S_V = 2P_L \quad (3.2)$$

Where  $P_L$  is the total number of intersections the desired phase has with the line / circle per unit length.

$P_L$  was calculated using intersections with line at low magnification, using the optical microscope, because at low magnification the phases appear to be randomly oriented. But for the high magnification study, where the orientation of phases was prominent, it was felt that calculations made using intersections with circles would be more feasible to accord for the orientations.

The interlamellar spacing of pearlite was also measured by the use of stereological concepts. Random lines were drawn on the micrographs having the pearlite structure and the true interlamellar spacing,  $\sigma_L$ , was calculated by using the mathematical relation given by equation 3.3.

$$\sigma_L = 1 / 2N_L \quad (3.3)$$

Where  $N_L$  is the total number of alternate cementite (or ferrite) plate intersected per unit length of the random lines drawn on the micrograph.

The measurements made using concepts of stereology were related to the changes occurring in samples taken from along the length of TSC1 and TSC2 rods and the thermo mechanically treated rods were characterized in relation to it. The volume fraction measurements made acted as a guideline to the mechanical results to be expected. X-ray diffraction was also carried out to know the total volume fraction of ferrite (present in the samples irrespective of whether it is present as polygonal ferrite or in bainite) and carbides.

### 3.5 X-Ray Diffraction

Some samples were also subjected to x-ray diffraction, using Seifert - ISO-DEBYFLEX 2002 diffractrometer. An attempt was made to confirm the phases present in different

samples and to estimate ferrite and cementite volume fraction of some samples using x-ray diffraction technique to verify the results obtained by stereology. The samples used for x-ray analysis were in form of plates of thickness around 1cm. The tube was operated at 30 KV and 20 mA and the radiation used was Cu -K $\alpha$ . In making the required calculations, knowledge of the theoretical intensity that will be observed at different 2 $\theta$  values should be known. The procedure involved for calculating the relative integrated intensity is discussed below.

The respective peaks were indexed and identified. The volume fraction of the respective phases in the samples was related to the intensity of the observed peaks.

Relative integrated intensity (I) is given by equation 3.4.

$$I = |F|^2 * p * L_P * T_F \quad (3.4)$$

Where 'F' is the structure factor and is independent of the shape and size of the unit cell. Structure factor for the hkl reflection is given by equation. 3.5

$$F_{hkl} = \sum_{j=1}^N f_n e^{2\pi(hu_n + kv_n + lw_n)} \quad (3.5)$$

Structure factor is the resultant of scattering by the unit cell containing atoms 1,2,3,4...N, with fractional coordinates  $u_1v_1w_1$ ,  $u_2v_2w_2$ ,  $u_3v_3w_3$  .....and atomic scattering factors  $f_1$ ,  $f_2$ ,  $f_3$ ; p is the multiplicity factor that accounts for the relative proportion of planes contributing to the same reflection, which is because of the fact that different planes have the same spacing;  $L_P$  in equation 3.4 is the Lorentz Polarization factor. The polarization factor is common for all samples and it accounts for having an unpolarized incident X-ray beam. The Lorentz factor depends on the diffraction geometry and is different for powder samples (equation. 3.6) and plate samples (3.7).

$$L_P = (1 + \cos^2 2\theta) / (\sin^2 \theta * \cos \theta) \quad (3.6)$$

$$L_P = (1 + \cos^2 2\theta) / (\sin 2\theta) \quad (3.7)$$

$T_F$  in the equation 3.4 is the Debye-Waller factor and accounts for the change in the intensity of the diffracted beam under the influence of thermal agitation. For samples in form of powder, its effect is cancelled by the opposing effect caused by another factor, absorption factor. So for the powder sample this factor can be neglected. If plate samples are being used,  $T_F$  is given by equation 3.8.

$$T_F = \exp(-B \sin^2 \theta / \lambda^2) \quad (3.8)$$



B is the temperature factor contributed by each atom and it is assumed that the value of B is same for all the atoms.

The calculation of the structure factor requires knowledge of the crystal structure of ferrite and cementite and co-ordinates of the atoms. Ferrite has a BCC structure and has two atoms of the same kind per unit cell located at  $(0,0,0)$  and  $(\frac{1}{2}, \frac{1}{2}, 0)$ . The crystal structure of cementite ( $\text{Fe}_3\text{C}$ ) is simple orthorhombic and has 12 iron (Fe) atoms and 4 carbon (C) atoms per unit cell. The co-ordinates of the 16 atoms in  $\text{Fe}_3\text{C}$  are given in table.3.2

The structure factor was calculated for ferrite and cementite using equation 3.2. Hence the theoretical integrated intensity was calculated for different hkl planes and is shown in table 3.3.

**Table 3.2:** Coordinates of atoms of cementite.

| Atom | u      | v     | w      |
|------|--------|-------|--------|
| C    | 0.89   | 0.25  | 0.45   |
| C    | -0.89  | 0.75  | -0.45  |
| C    | -0.39  | 0.75  | 0.95   |
| C    | 0.39   | 0.25  | 0.05   |
| Fe   | 0.036  | 0.25  | 0.852  |
| Fe   | -0.036 | 0.75  | -0.852 |
| Fe   | 0.464  | 0.75  | 0.352  |
| Fe   | 0.536  | 0.25  | -0.352 |
| Fe   | 0.186  | 0.063 | 0.328  |
| Fe   | -0.186 | -0.06 | -0.328 |
| Fe   | 0.686  | 0.437 | 0.172  |
| Fe   | -0.686 | -0.44 | -0.172 |
| Fe   | -0.186 | 0.563 | -0.328 |
| Fe   | 0.186  | -0.56 | 0.328  |
| Fe   | 0.314  | -0.06 | 0.828  |
| Fe   | -0.314 | 0.063 | -0.828 |

**Table 3.2** Theoretical intensities Obtained with Cu-K $\alpha$  Radiation at different hkl planes

| h | k | l | I <sub>CEMENTITE</sub> | $\frac{I_{CEMENTITE}}{I_{MAX}}$ | I <sub>FERRITE</sub> | $\frac{I_{FERRITE}}{I_{MAX}}$ |
|---|---|---|------------------------|---------------------------------|----------------------|-------------------------------|
| 1 | 0 | 0 | 6.31E-32               | 6.67E-31                        | 2.16E-31             | 3.88E-31                      |
| 1 | 1 | 0 | 0.000286               | 3.02E-03                        | 55.78097             | 100                           |
| 1 | 1 | 1 | 0.058586               | 6.19E-01                        | 7.55E-31             | 1.35E-30                      |
| 1 | 2 | 0 | 0.00102                | 1.08E-02                        | 1.2E-30              | 2.15E-30                      |
| 1 | 1 | 2 | 4.988901               | 5.27E+01                        | 29.26956             | 52.47231                      |
| 1 | 2 | 2 | 2.102914               | 2.22E+01                        | 2.36E-30             | 4.24E-30                      |
| 2 | 0 | 0 | 0.282667               | 2.99E+00                        | 11.77133             | 21.10277                      |
| 2 | 2 | 0 | 6.205488               | 6.56E+01                        | 12.3209              | 22.08799                      |
| 2 | 2 | 2 | 1.01182                | 1.07E+01                        | 13.53483             | 24.26424                      |
| 1 | 3 | 0 | 0.001404               | 1.48E-02                        | 27.4671              | 49.24099                      |
| 1 | 2 | 3 | 2.806452               | 2.97E+01                        | ---                  | ---                           |
| 2 | 3 | 0 | 1.103663               | 1.17E+01                        | 5.89E-30             | 1.06E-29                      |
| 2 | 2 | 3 | 0.024671               | 2.61E-01                        | ---                  | ---                           |
| 2 | 3 | 3 | 0.144209               | 1.52E+00                        | ---                  | ---                           |
| 1 | 3 | 3 | 3.244274               | 3.43E+01                        | ---                  | ---                           |
| 1 | 1 | 3 | 0.394688               | 4.17E+00                        | 3E-30                | 5.38E-30                      |
| 0 | 2 | 0 | 0.149272               | 1.58E+00                        | 11.77133             | 21.10277                      |
| 1 | 2 | 1 | 2.590367               | 2.74E+01                        | 29.26956             | 52.47231                      |
| 2 | 1 | 0 | 1.612542               | 1.70E+01                        | 1.2E-30              | 2.15E-30                      |
| 0 | 0 | 2 | 1.766866               | 1.87E+01                        | 11.77133             | 21.10277                      |
| 2 | 0 | 1 | 1.559224               | 1.65E+01                        | 1.2E-30              | 2.15E-30                      |
| 2 | 1 | 1 | 5.030373               | 5.32E+01                        | 29.26956             | 52.47231                      |
| 1 | 0 | 2 | 5.062469               | 5.35E+01                        | 1.2E-30              | 2.15E-30                      |
| 2 | 2 | 0 | 2.045261               | 2.16E+01                        | 12.3209              | 22.08799                      |
| 0 | 3 | 1 | 9.460264               | 1.00E+02                        | 27.4671              | 49.24099                      |
| 1 | 1 | 2 | 4.988901               | 5.27E+01                        | 29.26956             | 52.47231                      |
| 0 | 2 | 2 | 0.56956                | 6.02E+00                        | 12.3209              | 22.08799                      |
| 1 | 3 | 1 | 2.909702               | 3.08E+01                        | 3E-30                | 5.38E-30                      |
| 2 | 2 | 1 | 4.602839               | 4.87E+01                        | 2.36E-30             | 4.24E-30                      |
| 1 | 2 | 2 | 2.102914               | 2.22E+01                        | 2.36E-30             | 4.24E-30                      |
| 2 | 0 | 2 | 0.308673               | 3.26E+00                        | 12.3209              | 22.08799                      |
| 2 | 3 | 0 | 1.103663               | 1.17E+01                        | 5.89E-30             | 1.06E-29                      |
| 2 | 1 | 2 | 0.576152               | 6.09E+00                        | 2.36E-30             | 4.24E-30                      |
| 3 | 0 | 1 | 1.795939               | 1.90E+01                        | 27.4671              | 49.24099                      |
| 2 | 3 | 1 | 0.302599               | 3.20E+00                        | ---                  | ---                           |
| 3 | 3 | 1 | 0.038645               | 4.09E-01                        | ---                  | ---                           |
| 1 | 3 | 2 | 0.272583               | 2.88E+00                        | ---                  | ---                           |
| 1 | 4 | 1 | 0.362187               | 3.83E+00                        | ---                  | ---                           |
| 3 | 2 | 1 | 0.01393                | 1.47E-01                        | ---                  | ---                           |
| 1 | 1 | 3 | 0.394688               | 4.17E+00                        | 3E-30                | 5.38E-30                      |
| 2 | 4 | 0 | 0.539611               | 5.70E+00                        | ---                  | ---                           |
| 2 | 3 | 2 | 0.304166               | 3.22E+00                        | ---                  | ---                           |
| 2 | 4 | 1 | 0.158219               | 1.67E+00                        | ---                  | ---                           |

|   |   |   |          |          |          |          |
|---|---|---|----------|----------|----------|----------|
| 1 | 2 | 3 | 2.806452 | 2.97E+01 | ---      | ---      |
| 2 | 0 | 3 | 0.092691 | 9.80E-01 | 5.89E-30 | 1.06E-29 |
| 0 | 5 | 1 | 0.442014 | 4.67E+00 | ---      | ---      |
| 3 | 2 | 2 | 0.924405 | 9.77E+00 | ---      | ---      |
| 0 | 3 | 3 | 0.001087 | 1.15E-02 | ---      | ---      |
| 4 | 0 | 1 | 2.770539 | 2.93E+01 | ---      | ---      |
| 1 | 3 | 3 | 3.244274 | 3.43E+01 | ---      | ---      |
| 4 | 1 | 1 | 0.291801 | 3.08E+00 | ---      | ---      |
| 2 | 4 | 2 | 0.044167 | 4.67E-01 | ---      | ---      |
| 2 | 5 | 0 | 1.243496 | 1.31E+01 | ---      | ---      |
| 3 | 3 | 2 | 3.961491 | 4.19E+01 | ---      | ---      |
| 3 | 4 | 1 | 0.267034 | 2.82E+00 | ---      | ---      |
| 2 | 5 | 1 | 2.994876 | 3.17E+01 | ---      | ---      |
| 0 | 0 | 4 | 0.510083 | 5.39E+00 | ---      | ---      |
| 1 | 5 | 2 | 2.178289 | 2.30E+01 | ---      | ---      |
| 3 | 0 | 3 | 2.708503 | 2.86E+01 | ---      | ---      |
| 0 | 6 | 0 | 1.311135 | 1.39E+01 | ---      | ---      |
| 4 | 2 | 0 | 0.131098 | 1.39E+00 | ---      | ---      |
| 4 | 5 | 1 | 0.310037 | 3.28E+00 | ---      | ---      |
| 3 | 1 | 3 | 0.499833 | 5.28E+00 | ---      | ---      |
| 0 | 3 | 0 | 0.000137 | 1.45E-03 | 2.13E-31 | 3.81E-31 |
| 3 | 1 | 0 | 8.71E-05 | 9.21E-04 | 27.4671  | 49.24099 |

### 3.6

#### Mechanical Testing

The thermomechanically treated rods were also characterized with respect to mechanical (hardness and tensile) properties. The significance of TSC1 and TSC2 treatment in comparison with quenching and tempering treatment was studied using mechanical tests. The significance of deformation temperature was evaluated by comparing mechanical properties of TSC1 and TSC2.

#### 3.6.1

##### Hardness measurements

The hardness of various phases was measured using a Leitz mini-load micro hardness tester. Microhardness was measured using the etched samples prepared for microscopy. The ferrite grain size of some samples along the rod was very less and so it became inconvenient to measure hardness of ferrite. If applied load was decreased to find its hardness, another problem arose. At lower load, it became a visual problem to measure

the indent on the dark bainitic constituent. So for convenience higher load of 0.49N was used for microhardness measurements of TSC1 and TSC2 samples. For the air-cooled samples also load of 0.49N was used. It was felt that macrohardness would be a more practical way of comparison of hardness of different samples, so Rockwell hardness tester was also used. Rockwell hardness of all the samples was found using 'C scale' (150 kg load and Brale indenter). Hardness measurement of differently thermomechanically treated samples was a good index of correlating the properties of two-step-cooling treatment with continuous cooling treatment.

### **3.6.2 Tensile Testing**

The unannealed TSC1 and TSC2 samples were difficult to machine, so finding tensile properties of unannealed samples was inconvenient. Hence annealed TSC1 and TSC2 samples were used for tensile tests. Tensile test on specimens, made as per ASTM E8, were done at an initial rate of  $5 \times 10^{-4}$  in strain control mode using a closed loop servo-hydraulic materials testing machine. With the progress of work it was realized that the position of the rod from which tensile test specimen was made is a very important factor to be observed for the tensile properties. So to study the tensile properties in relation to sample position in the forged rod, gage length was decreased from 30mm to 20mm but strain rate was maintained. The results of tensile tests performed for TSC, CC samples were compared and significance of each treatment was studied.

## **CHAPTER 4**

### **Results and Discussions**

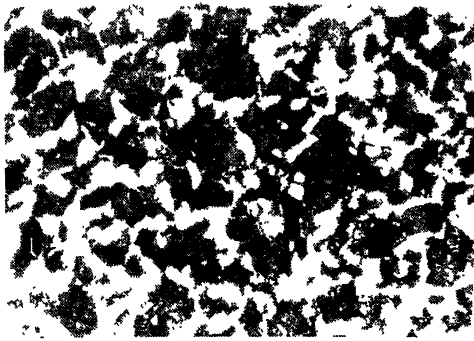
The thermomechanically treated 38MnSiVS6 microalloyed steel was characterized by various techniques already discussed in chapter 3. In the present investigation the response of air-cooled and two-step cooled treatment on the material was studied. The tensile results of quenched and tempered treatment were taken for the purpose of comparison with the other treatments.

#### **4.1 Microstructures**

The microstructures were studied and compared in order to understand the differences generated by the various treatments. The optical photographs provided the basic structural differences in the various samples. At low magnification the basic similarities and differences in differently treated samples were indicated while the SEM micrographs disclosed the high magnification features. Microstructural study was a very important tool in correlating the properties, obtained after different treatments, to the phases present in the structure.

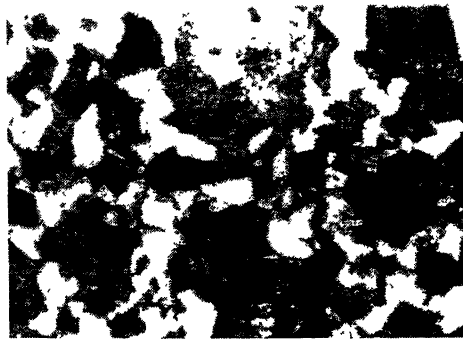
##### **4.1.1. Air Cooled**

The air-cooled rods had the typical pearlite–ferrite structure, shown in the micrographs of figure 4.1. There exists a microstructural variation along the length of the rod. At the extreme end the structure is very fine. As the length is transversed there is initially a gradual increase in the grain size and beyond a certain distance the grain size starts decreasing. It was observed that grains are coarsest at a distance of around 20 cm from the end. It can be seen from figure 4.1b and 4.1e that ferrite as well as pearlite grains are very coarse in the region. This observation can be explained by the combined effect of



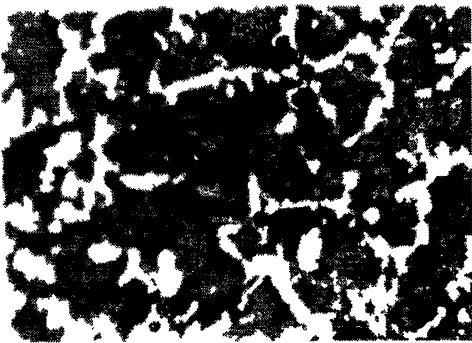
(a)

35μm



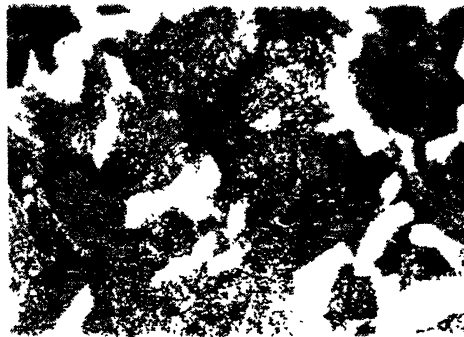
(d)

17μm



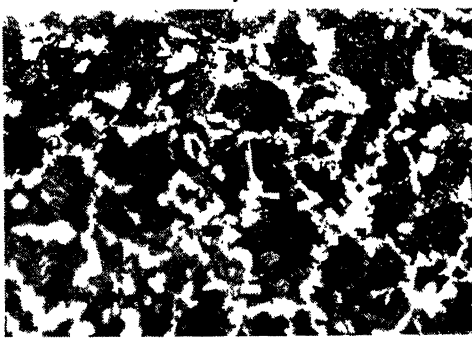
(b)

35μm



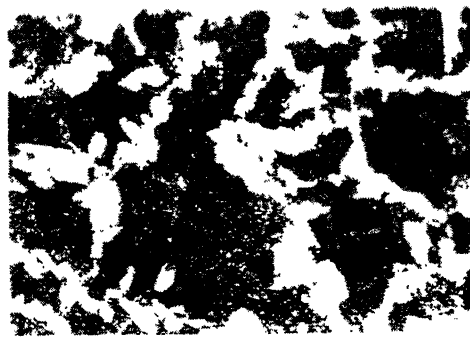
(e)

16μm



(c)

35μm



(f)

17μm

**Figure. 4.1 : Microstructure of air-cooled samples**

(a)&(d) : sample taken from 1 cm from end of the rod.

(b)&(e) : sample taken from 20 cm from end of the rod.

(c)&(f) : sample taken from 30 cm from end of the rod.

cooling rates and deformation (forging) induced on the sample. The cooling rate is maximum at the extreme end of the rod and it decreases as one progress from end to middle of the rod. This differential cooling rate results in a temperature gradient along the rod. Consequently deformation is imparted to the various regions of the rod at different temperature ranges. The final diameter of the rod was almost constant at all parts along the rod, which implies that the overall deformation was constant. The above variation leads to a gradient in grain size along the rod. The fine grains at the extreme end of the rod are the result of rapid cooling rate (relatively less deformation is given prior to transformation of austenite). While in the middle of the rod (where cooling rate is minimum) fine grains are due to the large deformation imparted to austenite, prior to transformation. Therefore, there exists a certain region where neither factor (i.e., cooling rate and deformation prior to transformation) dominates and hence coarse grains are obtained (figures 4.1(a), (b)).

In figure 4.2a the structure appears to be a composite of three distinct phases, the white phase corresponding to ferrite along with a gray phase and a very dark phase. The gray and dark areas are both pearlite. The dark region was observed at high magnification (Fig. 4.2b) but the structure could not be resolved. This is because in this region the ferrite-cementite lamellae are very fine. The microhardness of this dark phase was around 464 HV50, which was comparable to the microhardness shown by the gray region (400 HV50). The light gray phase, when observed at high magnification, had the conventional lamellar appearance.

It was seen that along the rod there exists a variation in interlamellar spacing,  $\sigma_L$  (calculated using equation 3.3 from chapter 3) of pearlite. At the extreme end of the air-cooled rod,  $\sigma_L$  is very small and as the center is approached  $\sigma_L$  gradually increases as shown in figure 4.3. The lamellas at extreme end of the rod are so fine that the measurement of  $\sigma_L$  even at a high magnification of 10,000X is not possible. But beyond a distance of 9 cm from the end,  $\sigma_L$  measurement could be done at 10,000X. The gradual change in  $\sigma_L$  as the length of rod is traveled is shown in table 4.1.

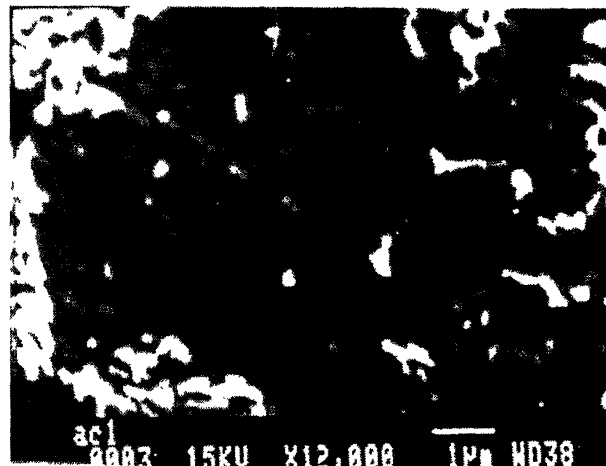
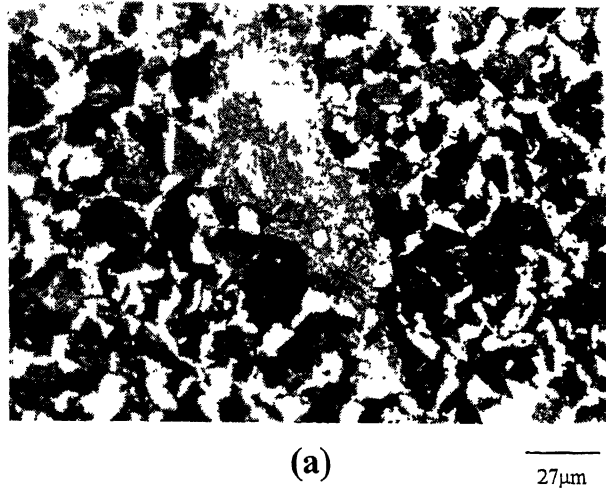
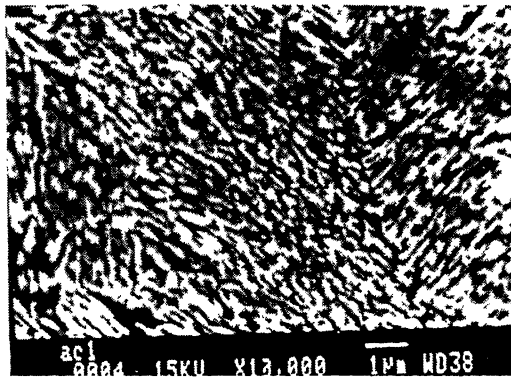
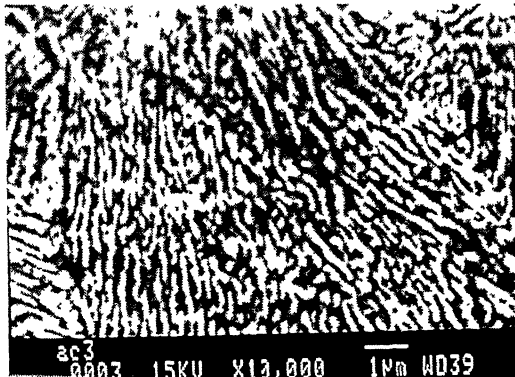


**Figure.4.2 : Microstructure of air-cooled sample**  
(a) at low magnification  
(b) the dark phase in (a) at high magnification.

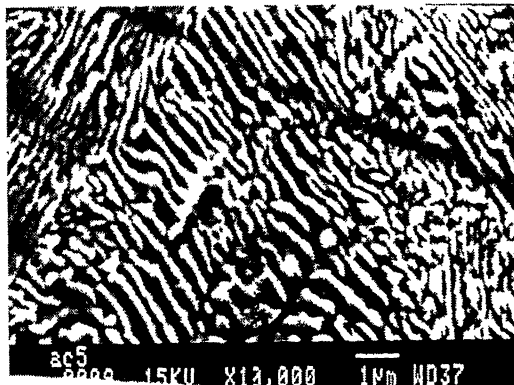




(a)



(b)



(c)

**Figure.4.3 : Microstructure of air-cooled samples at 10,000X**

- (a) sample taken from 1cm from end of the rod.
- (b) sample taken from 10 cm from end of the rod.
- (c) sample taken from 18 cm from end of the rod.

**Table 4.1:** Variation of interlamellar spacing along the length of rod.

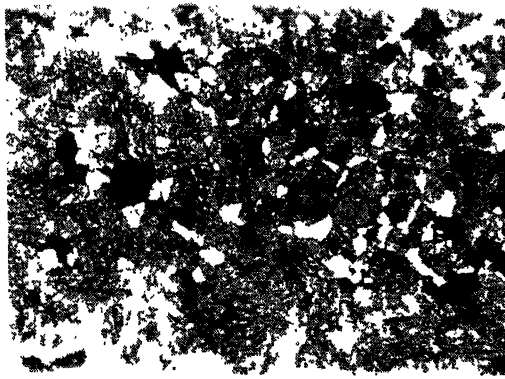
| S NO. | DISTANCE FROM<br>ONE END OF THE<br>ROD (cm) | INTERLAMMELAR<br>SPACING ( $\sigma_L$ ) IN mm<br>MEASURED AT 10,000X |
|-------|---|--|
| 1     | 1   | ---  |
| 2     | 5   | ---  |
| 3     | 9   | 1.16   |
| 4     | 13  | 1.49   |
| 5     | 17  | 1.96   |
| 6     | 21  | 2.05   |
| 7     | 25  | 2.12   |

The change in interlamellar spacing is because of the decrease in cooling rate from the end to center of the rod. At the extreme end of the rod, the rate of cooling is the maximum and hence results in very fine pearlite with low  $\sigma_L$ . As already discussed above, the grains are very fine at the end because of high cooling rate. Hence cooling rate is an important factor influencing the interlamellar spacing. Since the cooling rate is decreasing along the rod, interlamellar spacing of pearlite increases but the pearlite grain size shows maxima along the length of the rod at a distance of around 20 cm from the end. Only the cooling rate influences the interlamellar spacing while the pearlite colony size is a function of both the cooling rate and the deformation (forging) imparted to the rod prior to transformation from austenite.

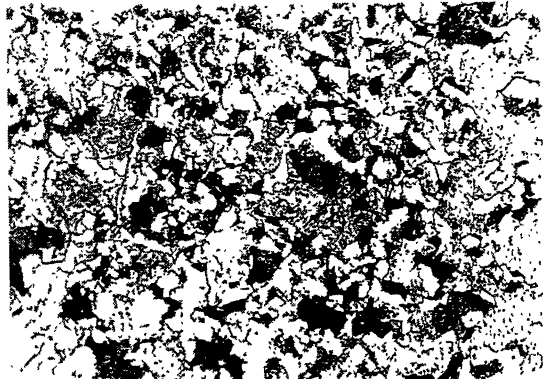
#### 4.1.2

##### Two-Step Cooled.

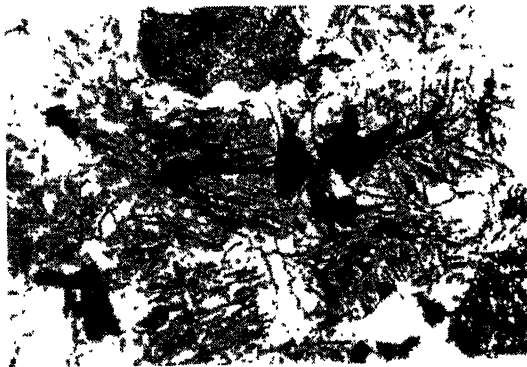
The microstructure of two-step cooled samples consisted of polygonal ferrite and bainite. In the two stage cooling, the first slow cooling step (still air) certain fraction of soft proeutectoid ferrite forms and the accelerated cooling (water quench) in the second step results in the bainite transformation. Since the bainitic ferrite morphology is lathlike, as observed in figure 4.4, the bainite is termed as lower bainite. However, there is some evidence that suggests the presence of scattered areas of martensite ( which will be



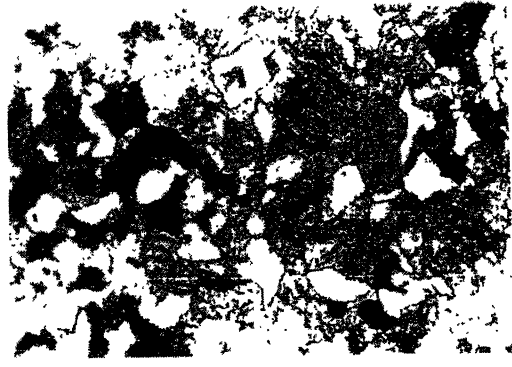
(a)



(c)



(b)



(d)

**Figure 4.4 : Microstructure of two-step cooled samples taken from extreme end of the rod.**

(a)& (b) : TSC1

(c) & (d) : TSC2

discussed in the following section). Thus, it may be concluded that microstructures of both TSC1 and TSC2 in figures 4.4, 4.5 are primarily composed of proeutectoid ferrite and lower bainite. For this particular grade of steel bainite start temperature ( $B_s$ ) calculated by using equation 2.7 was found to be  $580^{\circ}\text{C}$ . Thus it can be assumed that in the second accelerated cooling step transformation to lower bainite is the most preferred transformation.

On observing the optical microstructure along the rod it was found, for both TSC1 and TSC2, that at extreme ends of the rod there was a significant amount of polygonal ferrite present along with lower bainite, which decreases towards the middle of the rod. Finer and more homogeneous austenite microstructure at the start of austenite to ferrite transformation enhances the ferrite nucleation sites because of increased specific area of austenite grain boundaries and formation of deformation bands inside the grains. The grain size trend has already been discussed in section 2.1.1 and it directly corresponds to the ferrite content. Figures 4.4a and b if compared respectively with 4.4c and d show that TSC2 samples taken from the end of the rods have comparatively more ferrite content than TSC1 samples taken from the same position from the rod. The structure consisting of ferrite and bainite in TSC1 is coarser than in TSC2. This can be attributed to the fact that since TSC2 has a lower finish forging temperature than TSC1. It is possible that a certain amount of deformation out of the total amount of deformation imparted to TSC2 must be occurring below the recrystallization range. This increases the ferrite nucleation sites by introduction of deformation bands inside the austenite grains and resulting in an increase in ferrite nucleation rate.

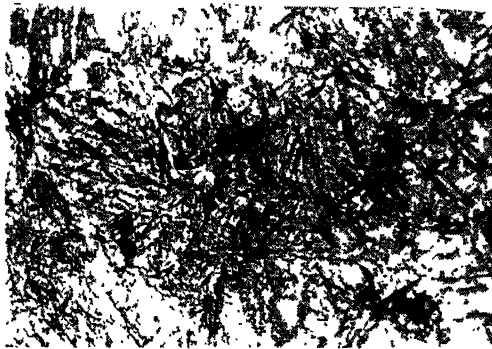
Along the length of the rod (total length was 60cm), it was found that beyond 10 cm distance from one end, the microstructure in both TSC1 and TSC2 rods tends to become uniform towards the center. From Fig 4.5 it can be seen that for samples taken from distance of 10 to 30 cms from one end, both TSC1 and TSC2 show almost similar optical microstructures with bainite present in TSC2 in a much finer form. Otherwise no significant microstructural dissimilarities can be observed in TSC1 and TSC2 samples using optical micrographs.



(a)  
TSC1 17μm



(d)  
TSC2 17μm



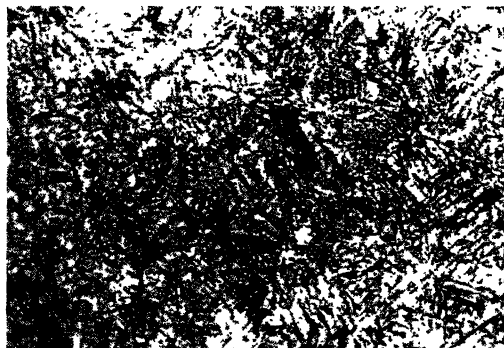
(b)  
TSC1 17μm



(e)  
TSC2 17μm



(c)  
TSC1 17μm



(f)  
TSC2 17μm

**Figure 4.5 : Microstructure of two – step cooled material .**

(a)&(d) : samples taken from 10 cm from end of the rod.

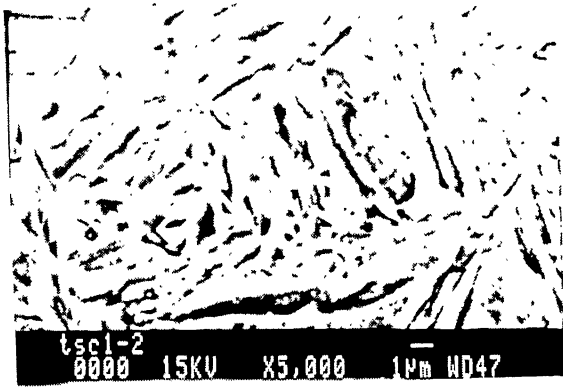
(b)&(e) : samples taken from 18 cm from end of the rod.

(c)&(f) : samples taken from 30 cm from end of the rod.

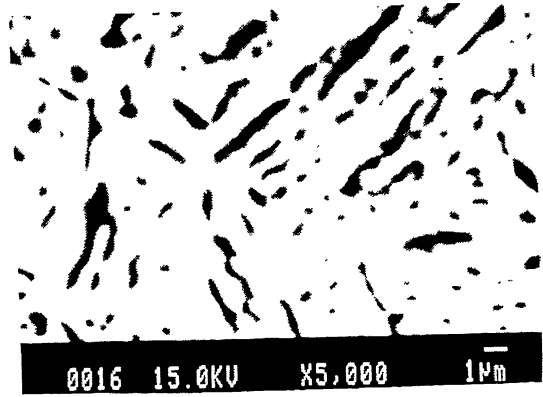
If the same samples are observed at high magnification in SEM, some major differences can be observed. SEM micrographs of two-step cooled samples in figures 4.6, 4.7, 4.8, 4.9 show the some finer features of bainite. From these it can be seen that ferrite and cementite exist in alternate manner. It has already been stated in section 2.3.5 that morphology of ferrite in bainite would be the criterion for defining the microstructure as upper or lower bainite. By observing the micrographs it was confirmed that the bainite present is lower bainite. Hence it can be assumed that all the microstructural features being observed in figs 4.6, 4.7, 4.8, 4.9, correspond to details of lower bainite.

The inspection of optical micrographs had yielded the result that TSC1 and TSC2 samples had similar microstructure barring the difference in ferrite volume fraction. But SEM micrographs show distinct differences in lower bainite features of TSC1 and TSC2 samples. Figure 4.6 shows TSC1 microstructure for samples taken from different positions along the rod, at magnification of 5000X. At the end of the rod the bainite appears to be very coarse. By observing the micrographs (figures 4.5c and d) it is seen that the bainite in the samples taken beyond 10 cm from one end of the rod to the center, appear similar.

In TSC2, at extreme end of the rod the bainite seems to be coarse as in TSC1. Though if figure 4.7 is observed, at magnification of 3500X and 5000X, the microstructure of both TSC1 and TSC2 appear to be similar. But the dissimilarities are quite evident at higher magnification of around 8000X or 10000X. It was observed in TSC2 that beyond a distance of around 15 cms from one end, the cementite plates are becoming continuous. In TSC2, samples taken at 4cm the end (Figs 4.8a & 4.9a) and 10cm from the end (Fig 4.8b & 4.9b), cementite is not continuous. However, samples taken rod at distance of 15 to 30 cm from the end (figures 4.8 & 4.9 (c), (d), (e)) show cementite bands to be, quite broad and continuous. While in TSC1, cementite bands are not continuous throughout the length of the rod. Micrographs of TSC1 at 10,000X (Fig. 4.7) depict the dissimilarity in the microstructure.



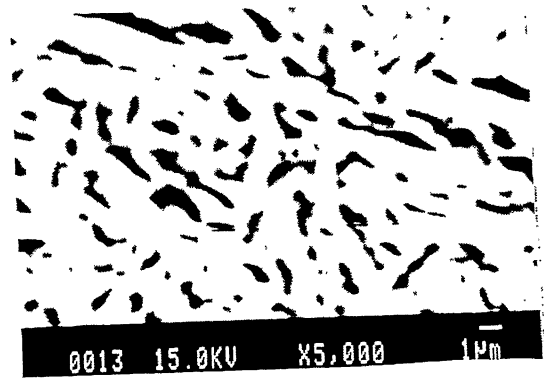
(a)



(c)



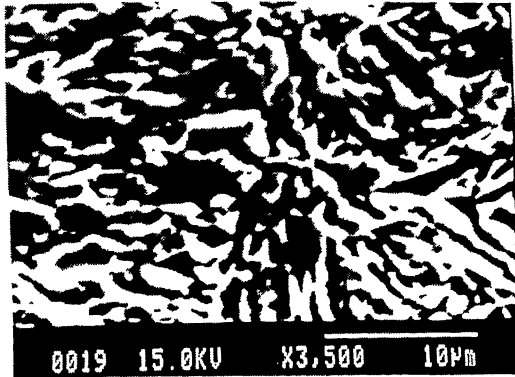
(b)



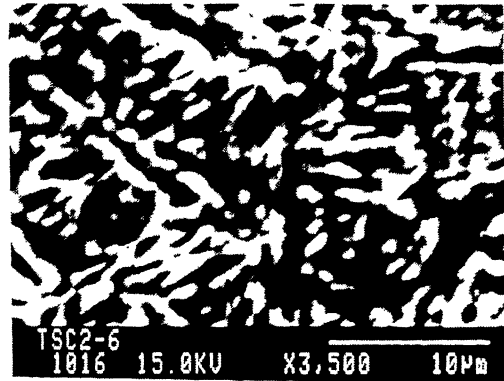
(d)

**Figure. 4.6 : Microstructures of TSC1 at 5000X.**

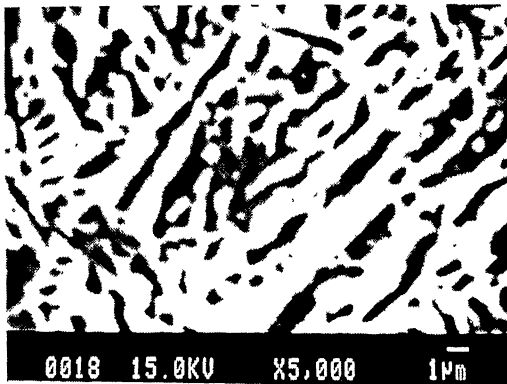
- (a) sample taken from 3 cm from the end of the rod.
- (b) sample taken from 8 cm from the end of the rod.
- (c) sample taken from 18 cm from the end of the rod.
- (d) sample taken from 30 cm from the end of the rod.



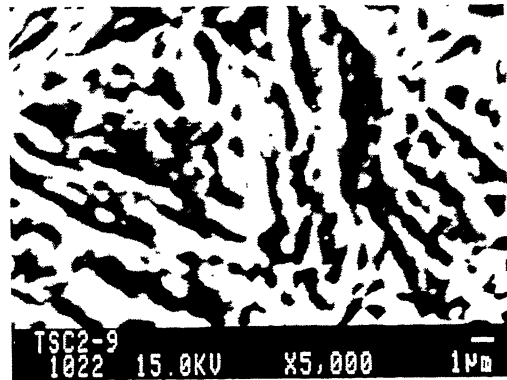
(a)  
TSC1



(c)  
TSC2



(b)  
TSC1



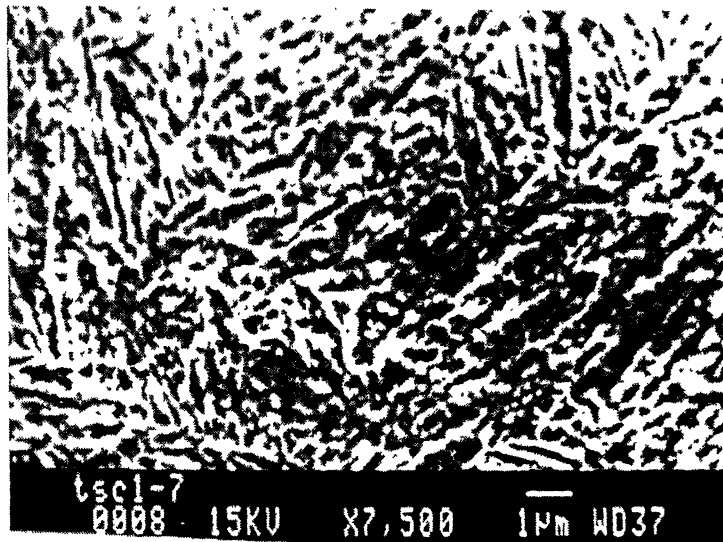
(d)  
TSC2

**Figure 4.7 : Comparison of microstructures of TSC1 and TSC2.**

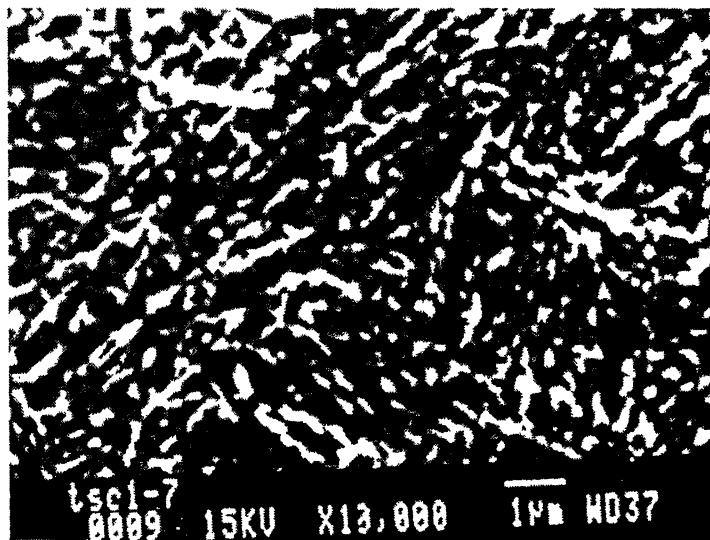
(a)&(c) : samples taken from 18 cm from end of the rod.

(b)&(d) : samples taken from 30 cm from end of the rod.



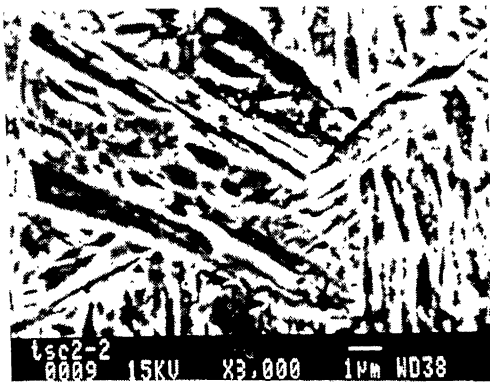


(a)

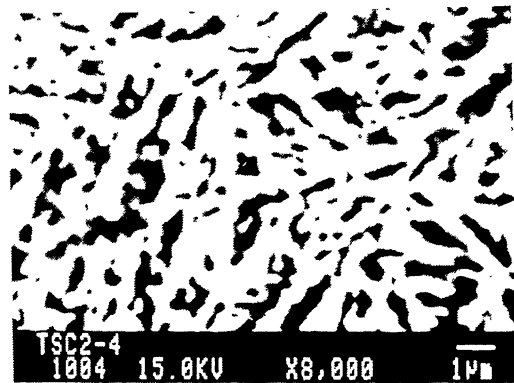


(b)

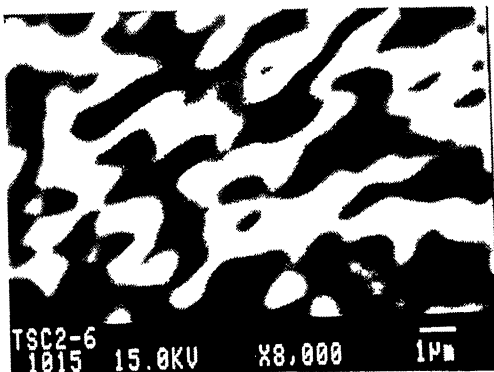
Figure 4.8 : Microstructure of TSC1 at 10,000X



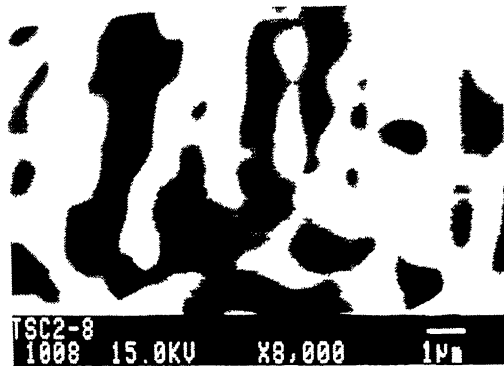
(a)



(b)



(c)



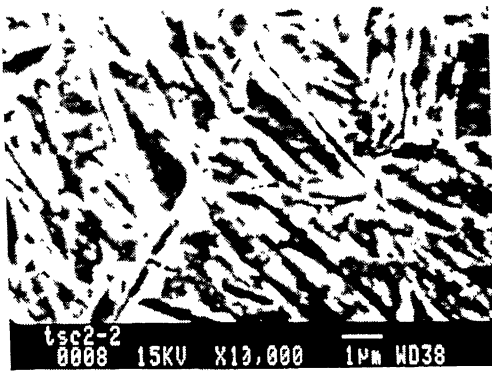
(d)



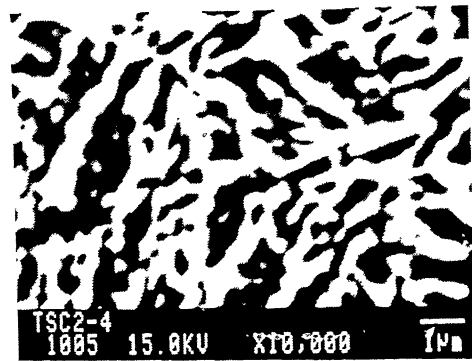
(e)

**Figure 4.8 : Microstructures of TSC2 at 8,000X**

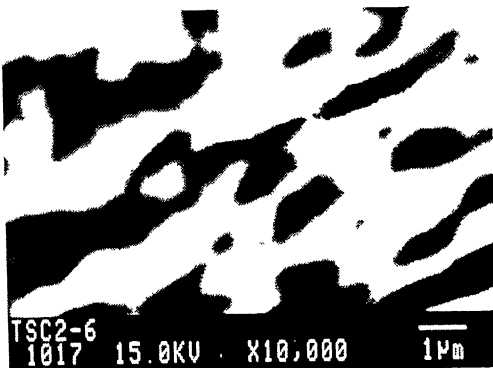
- (a) sample taken from 4cm from end of the rod.
- (b) sample taken from 10cm from end of the rod
- (c) sample taken from 18cm from end of the rod
- (d) sample taken from 25cm from end of the rod
- (e) sample taken from 30cm from end of the rod



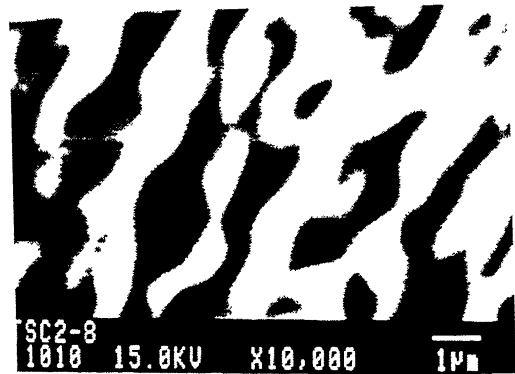
(a)



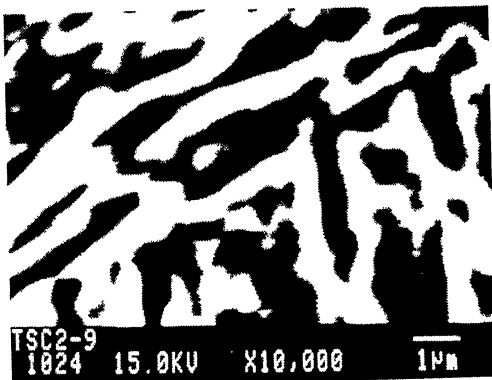
(b)



(c)



(d)



(e)

**Figure 4.9 : Microstructures of TSC2 at 10,000X**

- (a) sample taken from 4cm from end of the rod.
- (b) sample taken from 10cm from end of the rod
- (c) sample taken from 18cm from end of the rod
- (d) sample taken from 25cm from end of the rod
- (e) sample taken from 30cm from end of the rod

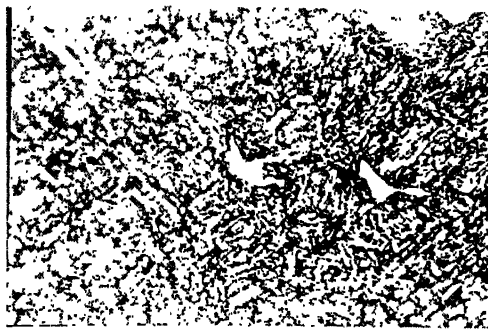
The continuity of cementite bands has been generally related to the percentage of carbon in the structure but this cannot be true in this case because the chemical composition of both TSC1 and TSC2 samples is the same. Thus, the difference in cementite morphology is attributed to the different thermomechanical treatment given to TSC1 and TSC2. The difference in finish forging temperature for TSC1 and TSC2 affects the bainitic transformation start temperature,  $B_s$  (580°C is the theoretical temperature  $B_s$  as calculated from equation 2.7) of both TSC1 and TSC2. This introduces difference in the kinetics and mechanism of bainite transformation in TSC1 and TSC2 and affects the manner in which cementite is precipitating. This probably leads to continuous cementite bands being observed in certain length of TSC2 and its total absence along the length of TSC1 rod. However, further investigation of this aspect is necessary.

#### **4.1.3**

#### **Annealed Structure of Two – Step Cooled Samples**

For practical reasons the samples for annealing were taken from 10 to 30 cm from the end since it was observed that in this region the microstructure appeared to be more homogeneous. The annealing was done at different temperature-400°C, 425°C, 450°C, 475°C, 500°C and for varying times of 1hr, 1.5 hrs, 2hrs and 2.5 hrs. It was seen that after annealing there was a distinct change in structure as compared to the unannealed ones. If the annealed micrographs in figure 4.10 are compared with unannealed micrographs shown in figure 4.4, it can be stated that with annealing the free ferrite in the structure increases and bainite appears have coarsened. This observation is true for both TSC1 and TSC2. From Figure 4.4 it can be observed that variation in the annealing temperature and time did not suggest any change in the microstructure of annealed two-step cooled samples.

The unannealed two-step cooled structures in figure 4.5 do not show any free ferrite but the same samples when annealed at 450°C show substantial fraction of free ferrite (figure 4.10). Bainitic ferrite usually contains only a slight excess of carbon in the solution thus the bainitic microstructures are less sensitive to annealing.



(a)  
400°C – 1.5 hrs



(d)  
400°C – 2.5 hrs



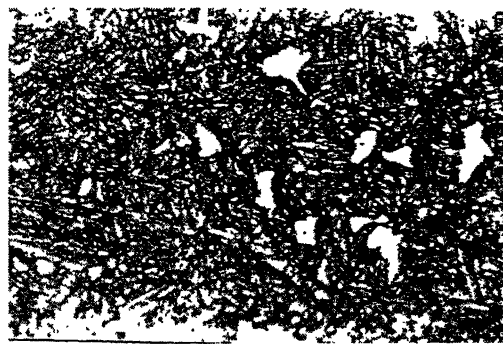
(b)  
425°C – 1.5 hrs



(e)  
425°C – 2.5 hrs



(c)  
475°C – 1.5 hrs



(f)  
475°C – 2.5 hrs

**Figure 4.10 : Microstructure of annealed two –step cooled material .**

(a),(b)&(c) : annealed TSC 1

(d),(e)&(f) : annealed TSC 2

Most of the carbon in annealed bainite is in form of cementite that tends to coarsen with the annealing treatment. In bainite only minor changes are to be observed as spheroidization and coarsening of cementite and hence presence of free ferrite in annealed samples cannot be related with annealed structure of bainite. It was observed (figure 4.11) that after annealing TSC2 samples taken from the end of the rod has comparatively higher volume fraction of free ferrite than annealed TSC1 samples, which can be attributed to the starting material being having higher ferrite fraction as explained in section 4.1.2.

The appearance of free ferrite can be attributed to the presence of small amounts of martensite in the two-step cooled samples, which could not be detected in the optical and scanning micrographs. During tempering the martensite present in the structure decomposes into ferrite and cementite. Hence along with the coarsened bainite, proeutectoid ferrite is observed.

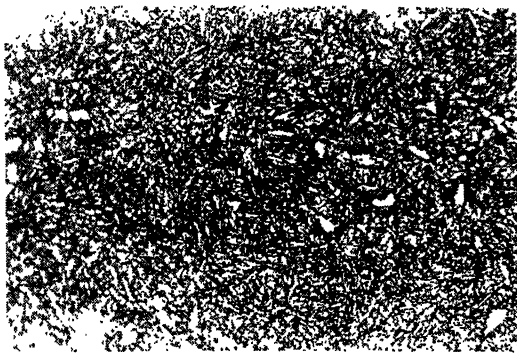
The annealed TSC1 and TSC2 microstructures were comparable as can be seen in Fig. 4.13. With high temperature annealing the discontinuous cementite bands in TSC1 coarsens to a considerable extent while the continuous cementite bands in TSC2 break and coarsen. Hence the structure that looked different before annealing starts appearing similar after annealing has been performed. Hence it can be inferred that the difference in finish forging temperature has no significant influence on the annealed microstructure of TSC1 and TSC2 observed.

The SEM micrographs (Fig 4.13) showed no variation in the microstructure with the changes in annealing temperature and confirm the observation made in optical micrographs. The micrographs illustrate the bainitic morphology after annealing and in this the coarsening of carbides after annealing is quite evident. In some of the micrographs (figures 4.12(b), (e)) the carbides are very coarse and the amount of bainitic ferrite is very less.

## **4.2**

### **Stereological Measurements**

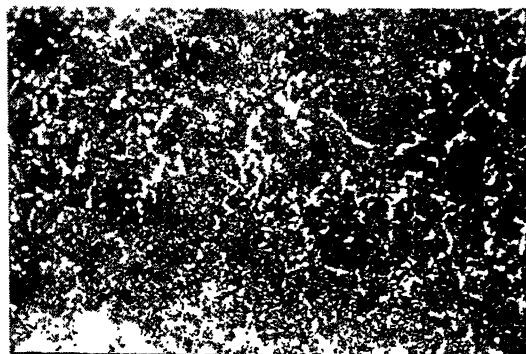
The qualitative differences observed in the microstructures of TSC1 and TSC2 were quantified by means of stereological methods as described in section 3.4 of chapter 3



(a)

77μm

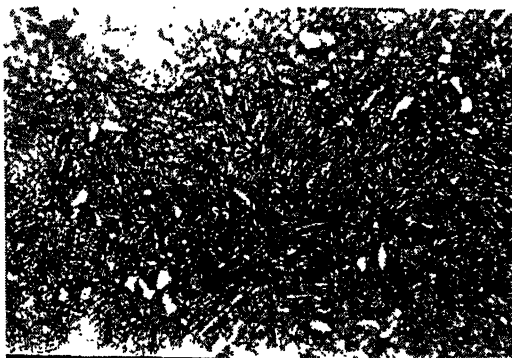
TSC1



(c)

77μm

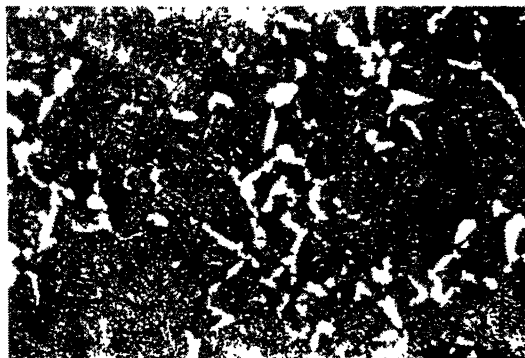
TSC2



(b)

31μm

TSC1

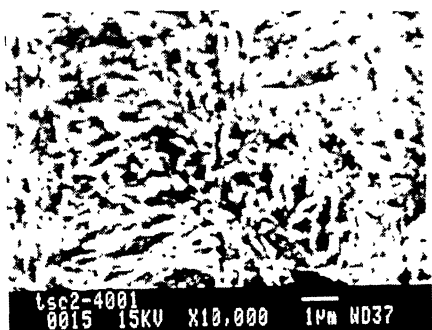


(d)

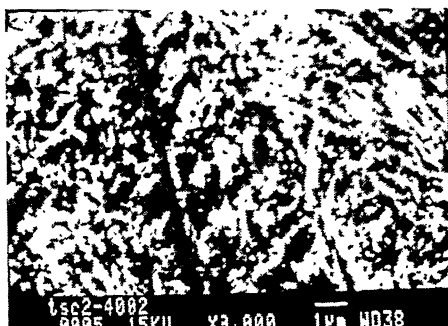
31μm

TSC2

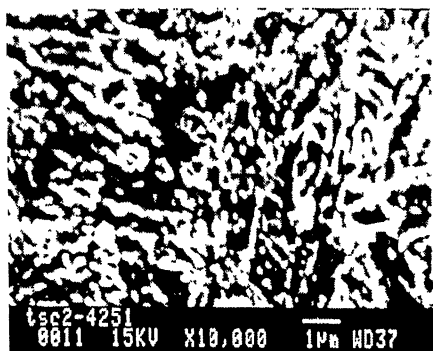
**Figure. 4.11 : Microstructure of two – step cooled samples annealed at 450° C for 1.5 hrs.**



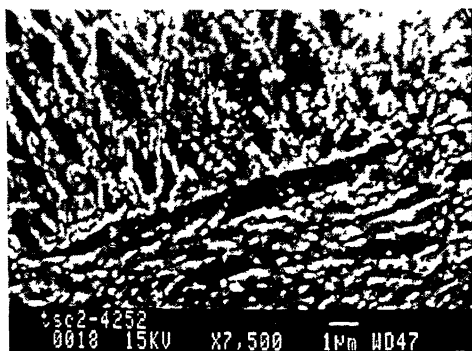
(a)



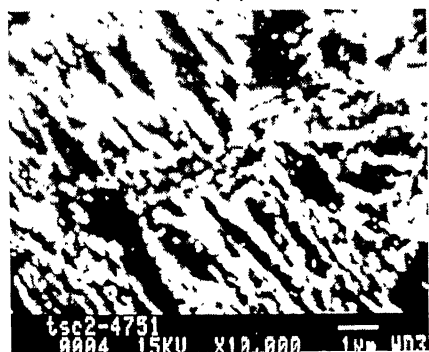
(d)



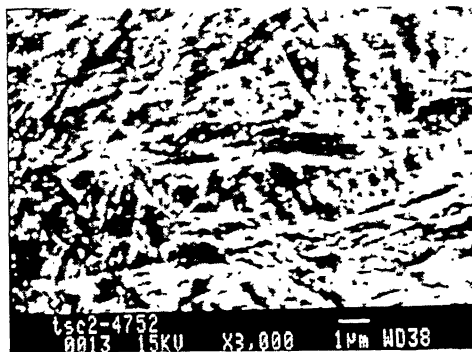
(b)



(e)



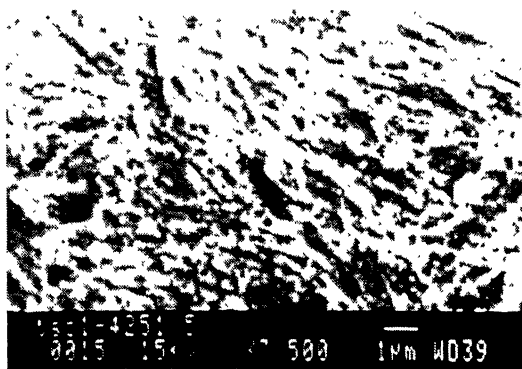
(c)



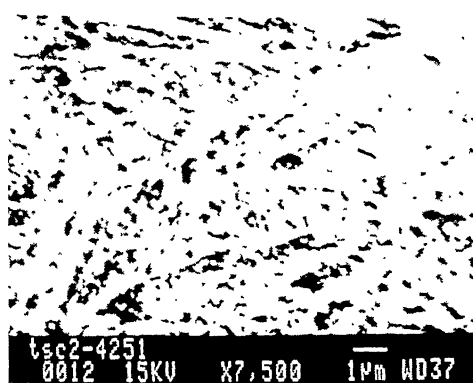
(f)

Figure. 4.12 : SEM Micrographs of Annealed TSC2





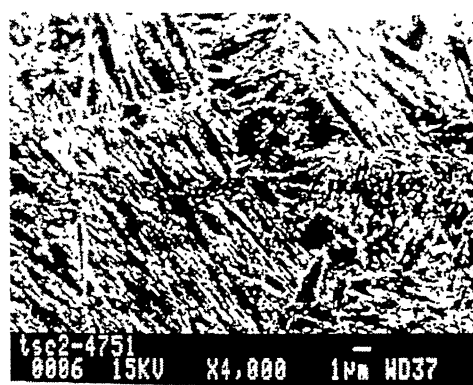
(a)  
TSC1



(c)  
TSC2



(b)  
TSC1



(d)  
TSC2

**Figure. 4.13 : Microstructures of annealed two – step cooled samples.**

(a)&(c) : samples annealed at 425°C.

(b)&(d) : samples annealed at 475°C.

Stereological measurements were done on SEM and optical micrographs as well as through suitable attachments in the microscope. It was observed that there exists a minimum in volume fraction of free ferrite in air-cooled and two-step cooled samples (figures 4.1, 4.4). This minimum exists in the distance range 10-15 cm from one end of the rod. The figure 4.14 shows that along all the thermomechanically treated, TSC1, TSC2 and air-cooled, rods of length around 60 cms, maximum ferrite fraction exists at the extreme end and it decreases gradually till a certain location and then increases towards the center of the rod. The trend observed for the volume fraction of the proeutectoid ferrite present along the length after all the imparted treatments, is shown in figure 4.14.

The minima in the free ferrite content can be explained the maxima observed in grain size. In section 4.1.1 it has already been referred that influence of cooling rate and the deformation occurring at different temperature along the rod leads to appearance of maxima in the grain size along the rod. The same factor is causing the minima in the ferrite volume fraction, along the length of the rod. The coarse austenite grains present in the certain region of the rod, have low specific grain boundary area and so have limited ferrite nucleation sites leading to low ferrite content in the region. From figure 4.14 it is evident that at all positions along the rod the volume fraction of proeutectoid ferrite content in TSC2 samples is greater than in TSC1 samples. The reason for this has already been discussed in section 4.1.2. TSC2 condition has lower finish forging temperature and hence TSC2 samples have been deformed till a lower temperature than the TSC1 samples. With low temperature deformation unrecrystallized austenite grains are elongated and have large specific grain boundary area and hence increased ferrite nucleation sites. So ferrite nucleation occurs on the grain boundaries and also in the deformation bands in the austenite grains. With intergranular and intragranular ferrite nucleation, the total ferrite content in TSC2 samples is higher than in TSC1 samples.

Volume fraction measurements were carried out for the cementite in bainite, at high magnification. From figure 4.15 it can be observed that maximum volume fraction of cementite occurs at the extreme end of the rod for both TSC1 and TSC2 and it decreases along the length of the rod. It has been explained in section 4.1.2 that cooling rate and the difference in temperature at which deformation (forging) is imparted to the rod affects the kinetics and mechanism of bainite transformation and the manner in which the cementite precipitates along the rod.

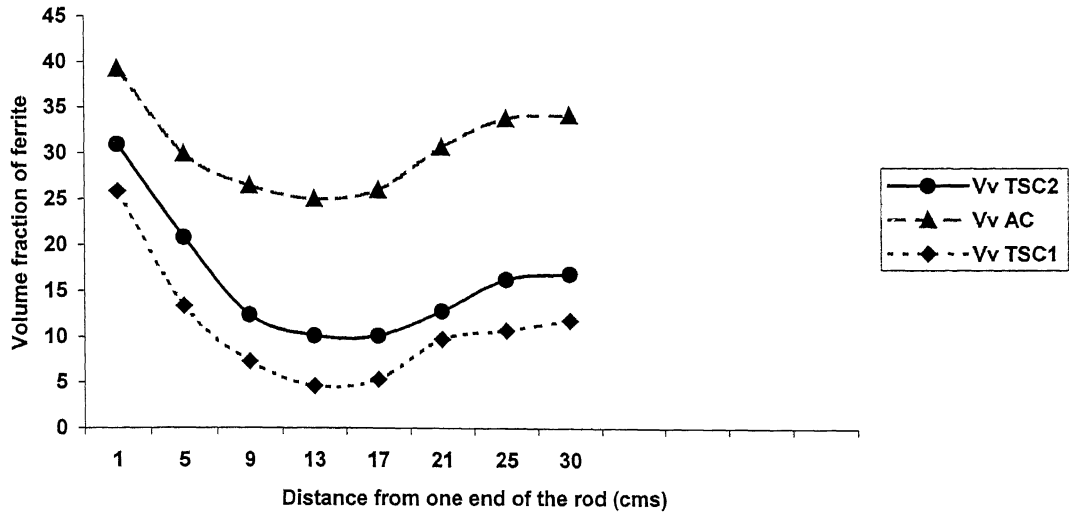


**Figure 4.14 :** Variation of proeutectoid ferrite content along the length of rod.

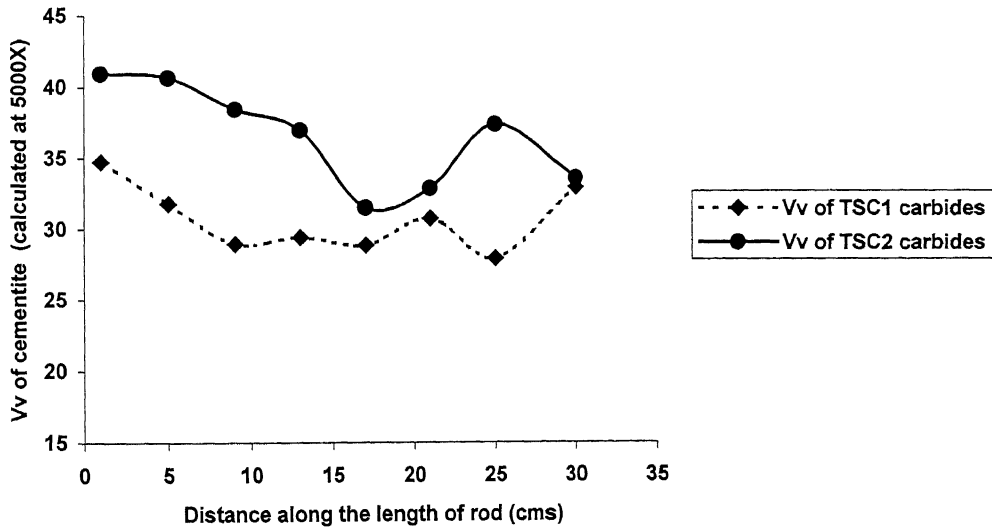


**Figure 4.15:** Variation of cementite (in bainite) along the length of rod.

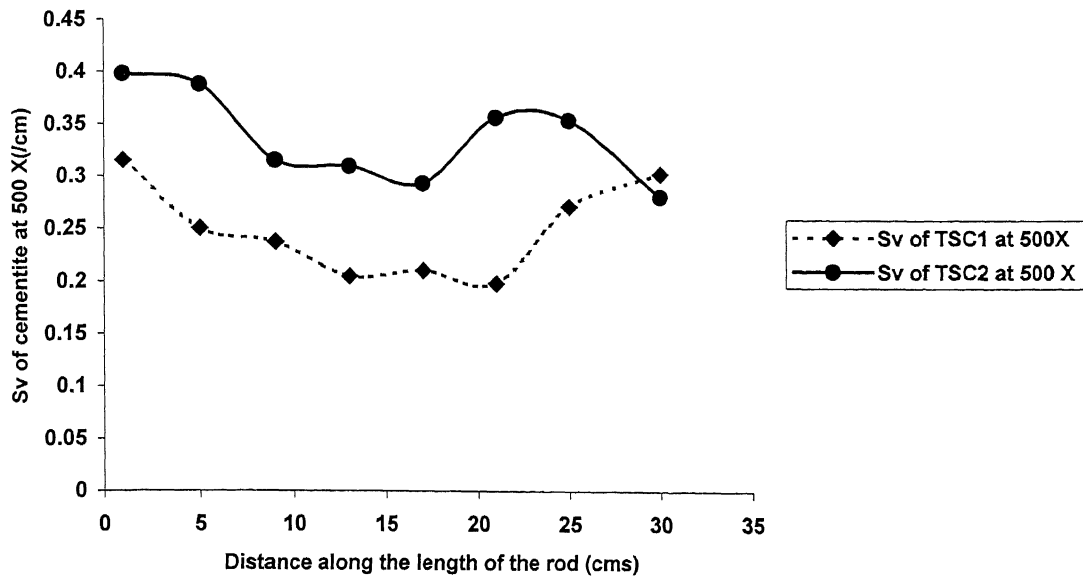
Hence the trend in figure 4.15 can be attributed to the way in which cementite is precipitating along the rod.

Surface area per unit volume,  $S_V$  (calculated using equation 3.3) of cementite at  $\alpha$ -Fe<sub>3</sub>C interface was measured at 500X and at 5000X (figures 4.16 (a) and (b)). It is seen that  $S_V$  at the extreme end of rod was higher for both TSC1 and TSC2. From figure 4.16(a) it can be observed that TSC2 samples have higher  $S_V$  than TSC1 throughout the rod. This can be credited to the presence of presence of finer grains in TSC2 material as compared to TSC1. From figure 4.16(b) it is observed that if SEM micrographs of TSC1 and TSC2 are used for  $S_V$  measurements no specific trend is seen along the rod. The absence of trend is due to unknown effect of influence of thermomechanical treatment on the cementite precipitation along the rod.

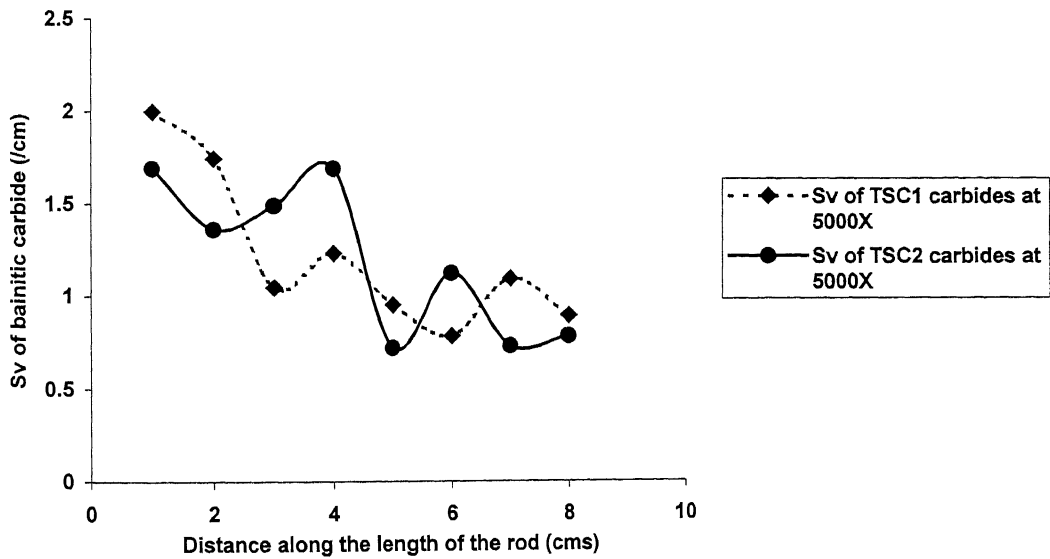
### 4.3

#### X-Ray Diffraction Results

The x-ray diffraction was carried out to identify the phases present and their volume fractions in different samples. The air-cooled sample, TSC samples (taken from end and center of the rods) and TSC samples annealed at different temperatures for 1.5 hrs, were subjected to x-rays diffraction. The representative x-ray plot is shown in figure 4.17. It can be seen that six peaks are obtained at different  $2\theta$  values. The main problem that arose during x-ray analysis was that no individual cementite peak was obtained and there were two overlapping ferrite–cementite peaks as shown in table 4.2. The table also mentions the respective hkl planes at which the peak is observed. It was observed that none of the peaks observed corresponds to the retained austenite peak. Generally with the martensite or bainite structure retained austenite is also present. Since in the investigation no austenite peak was obtained, it can be stated that the microstructure does not have any retained austenite. There is no separate martensite peak to confirm its presence in the structure. Martensite and ferrite peak overlap because the volume fraction of martensite is not enough to give a very distinct peak.



(a)



(b)

**Figure 4.16 :** Variation in surface area per unit volume of cementite along the rod.

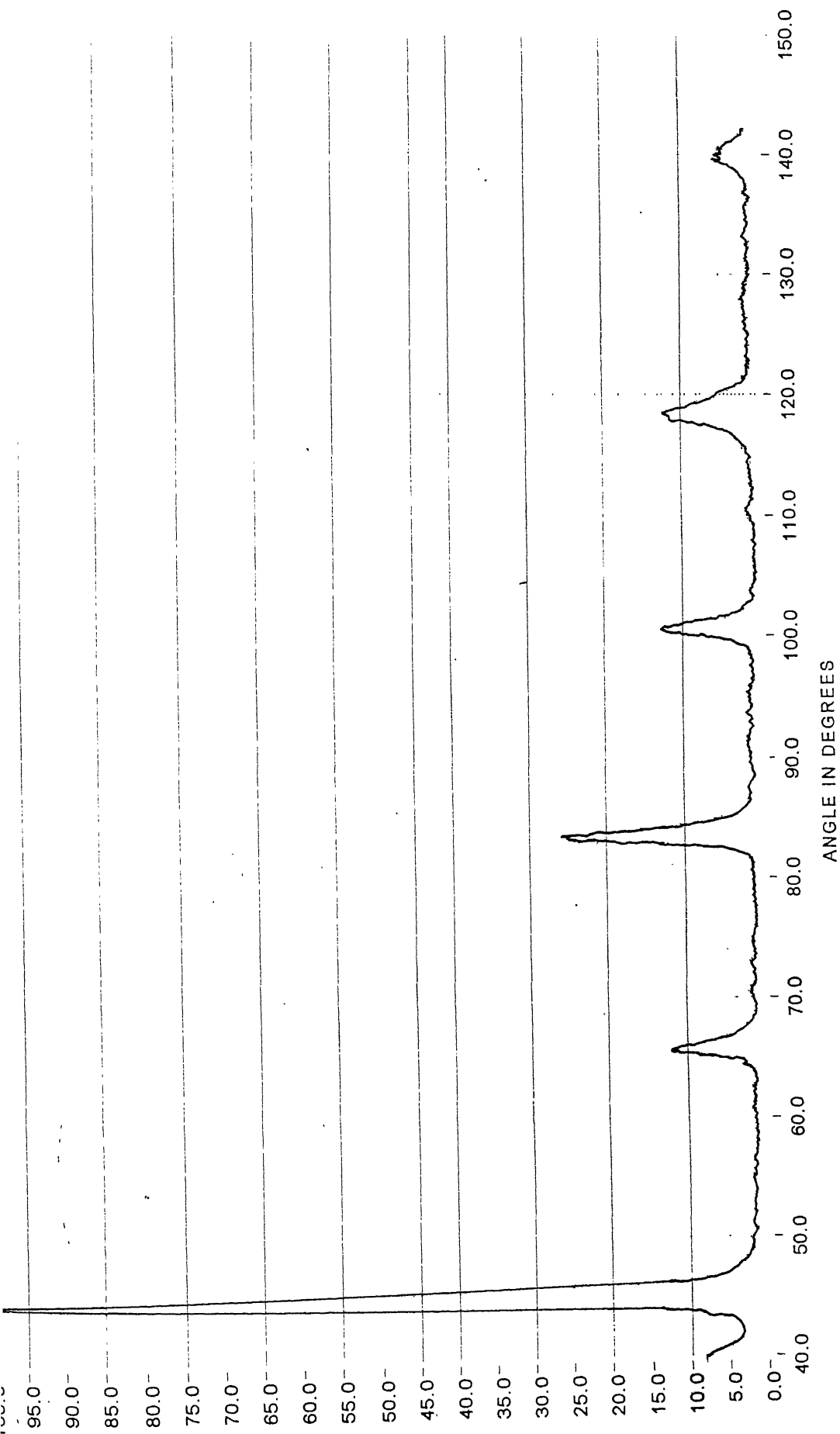


Figure 4.17 : Representative X-Ray Diffraction Plot of Two-Step Cooled Sample.

**Table 4.2:** Peaks Observed at  $2\theta$  for Cementite and Ferrite.

| ANGLE ( $2\theta$ )<br>in degrees | FERRITE          | CEMENTITE        |
|-----------------------------------|------------------|------------------|
| 45°                               | Peak at<br>(110) | Peak at<br>(031) |
| 65°                               | Peak at<br>(200) | X                |
| 82°                               | Peak at<br>(211) | Peak at<br>(332) |
| 99°                               | Peak at<br>(220) | X                |
| 117°                              | Peak at<br>(310) | X                |
| 137°                              | Peak at<br>(222) | X                |

The overlapping peaks of cementite and ferrite made the respective volume fraction calculation work little difficult because of the fact that the overlapping peaks are both high intensity peak as shown in table 3.3 (see section 3.3 for intensity calculations).

The volume fraction of the various phases was related to the observed integrated intensity of the peaks that correspond to the area under the peaks. Knowledge of actual intensity is necessary to accurately correlate the volume fraction to the intensity of the peak. An attempt was made to calculate the intensities of peaks corresponding to different hkl planes, for the samples to be examined in either as powder form or in plate form. The values of theoretical intensity to be observed at the  $2\theta$  values, at which peaks are seen, is taken from table 3.3 in chapter 3.

The theoretical intensity value for individual peaks was used to find the volume fraction of total ferrite (free ferrite as well as bainitic ferrite) and cementite. Equation 4.1 and equation 4.2 was used to calculate the volume fractions.

$$\frac{V_f^\alpha I_{\alpha_1} + V_f^{\text{Fe}_3\text{C}} I_{\text{Fe}_3\text{C}}}{V_f^\alpha I_{\alpha_2}} = \frac{I_{\alpha+\text{Fe}_3\text{C}}^0}{I_\alpha^0} \quad (4.1)$$

$$V_f^\alpha + V_f^{\text{Fe}_3\text{C}} = 1 \quad (4.2)$$

Where  $V_f^\alpha$  is the volume fraction of the ferrite phase,  $V_f^{\text{Fe}_3\text{C}}$  is the volume fraction of the cementite phase,  $I_{\alpha_1}$  is the theoretical intensity of ferrite at the combined ferrite-cementite peak, taken from table 3.2,  $I_{\text{Fe}_3\text{C}}$  is the theoretical intensity of cementite at the combined ferrite-cementite peak, taken from 3.2,  $I_{\alpha_2}$  is the theoretical intensity of ferrite at the individual ferrite peak, taken from table 3.3,  $I_{\alpha+\text{Fe}_3\text{C}}^0$  is the observed intensity of ferrite at the combined ferrite-cementite peak,  $I_\alpha^0$  is the observed intensity of ferrite at the individual ferrite peak.

The combined ferrite-cementite peaks observed at 45° and 82° were used for the calculations with the individual ferrite peaks observed at 65°, 99°, 117° and at 137°. For standardizing the procedure, equations 4.1 and 4.2 were used for different combinations of individual ferrite peaks and overlapping ferrite-cementite peaks. After the calculations it was observed that if the combined peak at 82° and individual ferrite peak at 99° is used in the equation 4.3.1, the results obtained showed a low percentage error. For all other peak combinations, the volume fraction data obtained was not harmonizing with the stereographic observations. The volume fraction data obtained by using combined peak at 82° and individual ferrite peak at 99° is tabulated in table. Since the information on transformation to bainite is insufficient to affirm the carbide-ferrite ratio in bainite, it is difficult to state the deviation of the calculated results from the actual values. The actual ferrite and pearlite volume fractions in air-cooled samples are known and with the theoretical ferrite cementite ratio of 8:1 in ferrite the total cementite volume fraction should have been around 0.1. Hence there is huge error associated with the calculated volume fraction for the air-cooled sample.

The errors obtained in the calculated volume fraction values can be attributed to many factors. Equation 4.1 was used for theoretical intensity calculation but this does not take into account the preferred orientation of ferrite and cementite in bainite (see section 2.3.5). The intensity equation 4.1 is derived on the premise of random orientation of the



constituent crystals in the samples. Deformation through forging may additionally introduce further texture in the material and certain hkl planes are preferentially present. The linear absorption coefficients for cementite ( $\mu_{\text{Fe}_3\text{C}} = 671.994$ ) and ferrite ( $\mu_{\alpha} = 2549.88$ ) are quite far apart. The incident beam passes through both cementite and ferrite. The intensity of beams passing decreased in intensity due to absorption by respective crystals. Since ferrite has a higher linear absorption coefficient value, the beam diffracted by the ferrite crystal could be much less than calculated. The effect of microabsorption by each diffracting ferrite crystal is not included in the basic intensity equation 4.1.

**Table 4.3:** Volume Fraction of Cementite as Obtained with X-Ray Diffraction.

| Material Condition  | Volume fraction of carbides<br>(Sample in plate form) |
|---|---|
| Air-cooled  | 0.4   |
| TSC1<br>Sample taken from end of the rod<br>Sample taken from center of the rod   | 0.27<br>0.36  |
| TSC2<br>Sample taken from end of the rod<br>Sample taken from center of the rod.  | 0.399<br>0.338  |
| TSC1A<br>Annealed at 400°C for 1.5hrs<br>Annealed at 425°C for 1.5hrs<br>Annealed at 450°C for 1.5hrs<br>Annealed at 475°C for 1.5hrs<br>Annealed at 500°C for 1.5hrs | 0.281<br>0.274<br>0.293<br>0.321<br>0.278             |
| TSC2A<br>Annealed at 400°C for 1.5hrs<br>Annealed at 425°C for 1.5hrs<br>Annealed at 450°C for 1.5hrs<br>Annealed at 475°C for 1.5hrs<br>Annealed at 500°C for 1.5hrs | 0.368<br>0.374<br>0.357<br>0.351<br>0.349             |

There is a large disparity in the ferrite and cementite grain size. This disparity in grain size affects the microabsorption by the respective crystals and hence affects the total intensity of the beam. More over the characteristic wavelength of radiation  $\text{Cu K}\alpha$  ( $=1.542 \text{ \AA}$ ) used was shorter than the K absorption edge of iron ( $=1.74334 \text{ \AA}$ ). This would cause fluorescence from the iron atoms in the specimen and the film may have become badly fogged, and erroneous results were observed.

#### **4.4**

#### **Mechanical Testing Results**

The observations made by microstructural study led to limited information on the dissimilarities introduced by the various treatments. The information gathered did not help in confirming the advantages of giving a particular treatment to the given material. The mechanical tests were the means to relate the microstructural observation to the mechanical properties and recognize the best thermomechanical treatment.

##### **4.4.1**

##### **Hardness Results**

The hardness of the different phases seen in the microstructure of various samples was measured using Vickers microhardness tester. It was observed that ferrite grains size was not large enough along the entire length of the rod, for microhardness measurements to be possible. Only at the extreme end, ferrite grains were large enough for microhardness measurements to be easily made. The hardness values of ferrite, shown in table 4.4 for unannealed TSC1 and TSC2 samples correspond to the samples taken from the extreme end of the rod. It can be seen that TSC2 samples have the largest hardness values of all the phases involved. The air-cooled samples have the lowest hardness as was expected according to its ferritic-pearlite microstructure. TSC2 is showing higher hardness levels which is quite surprising because it has higher amount of the soft phase, ferrite. TSC2 is deformed at a lower finish forging temperature than TSC1. The increased hardness is because ferrite formed has higher carbon content in it, since its formation is thermomechanically induced at a comparatively elevated temperature because of deformation at a lower temperature [3]. The enhanced ferrite formed in TSC2 rejects carbon in the adjoining austenite, which stabilizes the residual austenite. This

promotes the formation of bainite at lower temperature, which also shows higher hardness.

Annealing of TSC1 and TSC2 samples results in an increase in the hardness of polygonal ferrite (instead of decrease which would be normally expected) as can be verified from the table 4.4. The hardness of ferrite in TSC1 and TSC2 samples that have been annealed

**Table 4.4** Comparison of Hardness of two-step cooled condition.

| Material condition                             | Microstructure | Microhardness(HV50) |
|--|----------------|---------------------|
| Two-step cooling1(TSC1)                        | Bainite        | 700-760             |
|  | Ferrite        | 273-298             |
| Two-step cooling1(TSC1)<br>+Annealing (TSC1A)  | Bainite        | 456-480             |
|  | Ferrite        | 267-297             |
| Two-step cooling2 (TSC2)                       | Bainite        | 783-813             |
|  | Ferrite        | 300-343             |
| Two-step cooling2 (TSC1)<br>+Annealing (TSC2A) | Bainite        | 442-498             |
|  | Ferrite        | 276-290             |

show comparable hardness. This observation attributes to the fact that the material has vanadium as a microalloying addition, which precipitates as vanadium carbides in ferrite on annealing and increases its hardness. Bainite phase shows a decrease in hardness after annealing because of the coarsening of cementite during annealing as was reported in section 4.1.3 (Figs 4.10 to 4.13).

The hardness of TSC1 and TSC2 samples were measured along the length of the rod. Ferrite hardness could not be measured because of its fine size. The hardness trend seen in Fig 4.19 corresponds to bainite hardness as a function of distance along the rod. It was observed that though TSC1 and TSC2 microstructures appeared to be almost similar (Fig 4.5) but TSC2 has higher hardness than TSC1 at all points along the rod. This is attributed to the fact that the TSC2 was deformed to lower finish forging temperature. It has been explained in section 2.1.2 that TSC2 material had finer grains. TSC2 rods also showed continuous cementite bands in certain section of the rod. The variation in the microstructural observation attributes to high hardness. It can be seen from the figure

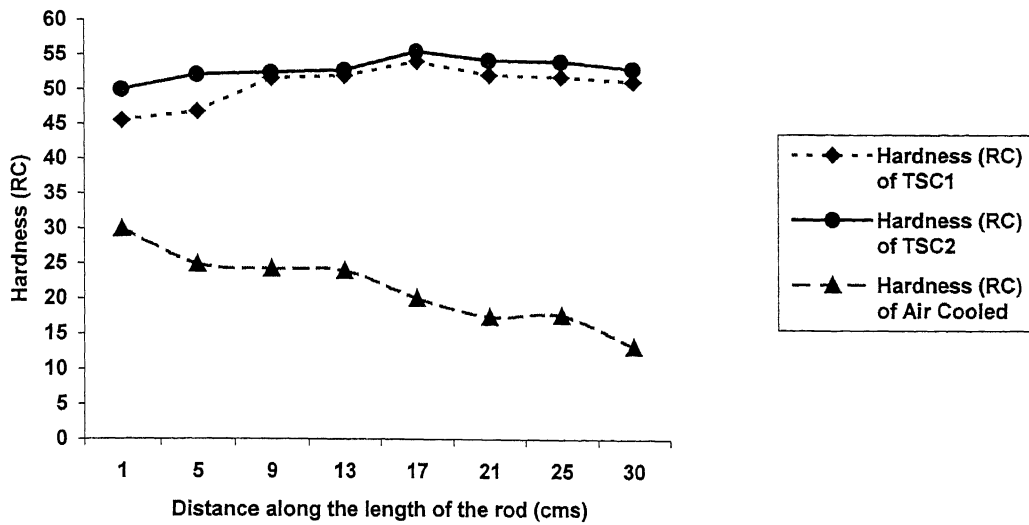


**Figure 4.18:** variation of hardness (RC) along the length of the thermomechanically treated rod.

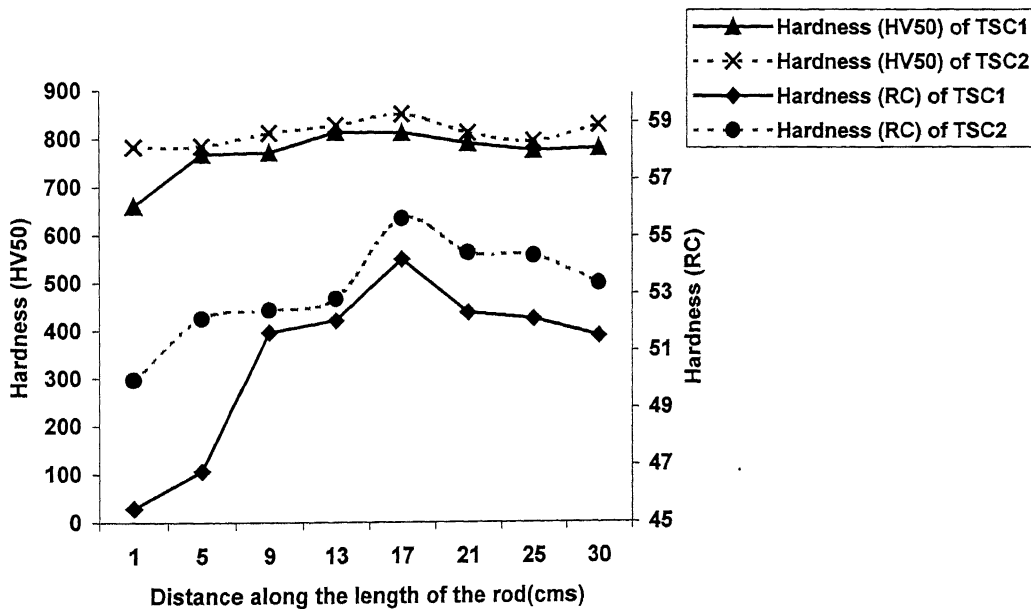


**Figure 4.19 :** Variation of hardness of two-step cooled samples along the rod.

4.19 that for both TSC1 and TSC2, as the length of the rod is traveled the hardness gradually increases.

The Rockwell hardness values also increases along the rod along the length of the rod for two-step cooled samples as is observed in figure 4.18. This observation can be related to the way in which the rods were being forged. Due to gradient in the cooling rate the deformation was imparted in different temperature range. The central region had minimum cooling rate and austenite was largely deformed prior to deformation. Hence fine transformed grains are obtained because of large deformation imparted in the region and hence increase in hardness along the rod is observed. For the air cooled samples there is gradual decrease in the hardness values along the length of the rod. This can be related to the fact that in air-cooled samples the interlammellar spacing of pearlite is increasing as the center of the rod is approached. Finer pearlite imparts high hardness to the structure.

It was observed that there is a definite decrease in the hardness values with annealing of two-step cooled samples. The ferrite content increases with annealing along with coarsening of cementite, which attributes to the decrease in hardness. However, there is no significant effect of change in annealing temperature and time on the hardness.

#### **4.4.2 Tensile Tests**

The tensile tests were performed to judge the superiority of mechanical properties of the various treatments. The tests gave information about ductility, strength and toughness values of differently treated samples. The tensile properties of the four heat-treated conditions – air-cooled, TSC1 annealed (TSC1A), TSC2 annealed (TSC2A) and quenched and tempered (Q&T) are reported in table 4.5. The results for quenched and tempered condition is only included for comparison. The properties corresponding to TSC1A and TSC2A conditions are after annealing at 450°C for 1.5 hrs. Optimal properties for Q&T condition was obtained when tempering was done at 550°C for 1.5 hrs. The variation of hardness, strength and ductility with variation in annealing temperature, keeping annealing time constant at 1.5 hrs, is shown in figure 4.20.

The 0.2% proof stress and the ultimate tensile strength (UTS) are higher for TSC1 than TSC2 but the percentage elongation was lower for TSC1 compared with TSC2. The

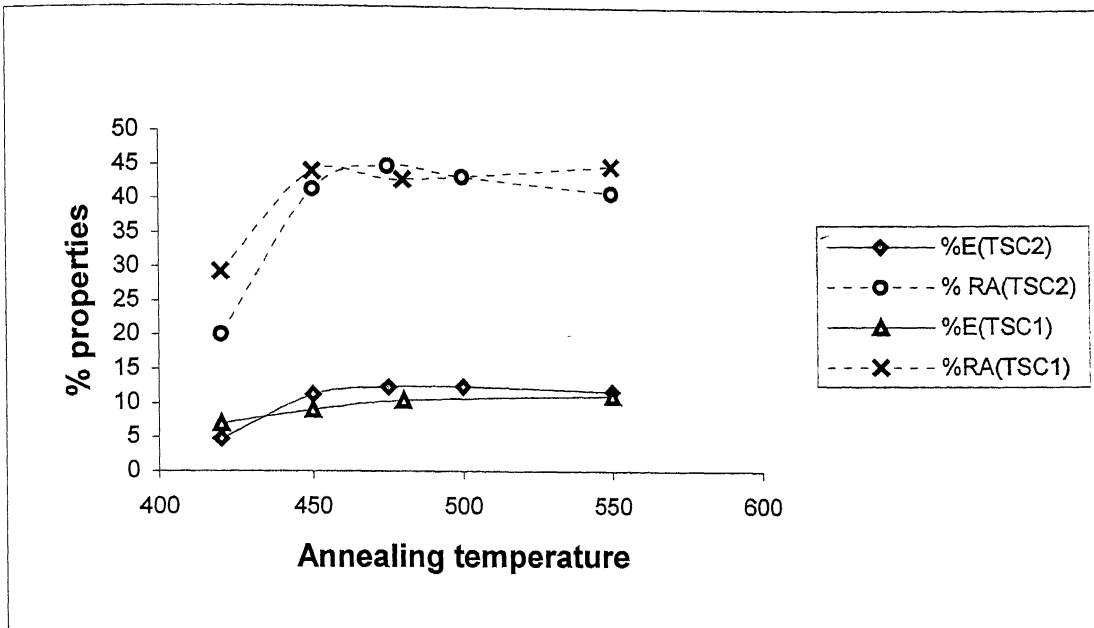


**Figure 4.20a:** Effect of annealing temperature on % Elongation (E) and % Reduction in area (RA) of TSC1 and TSC2

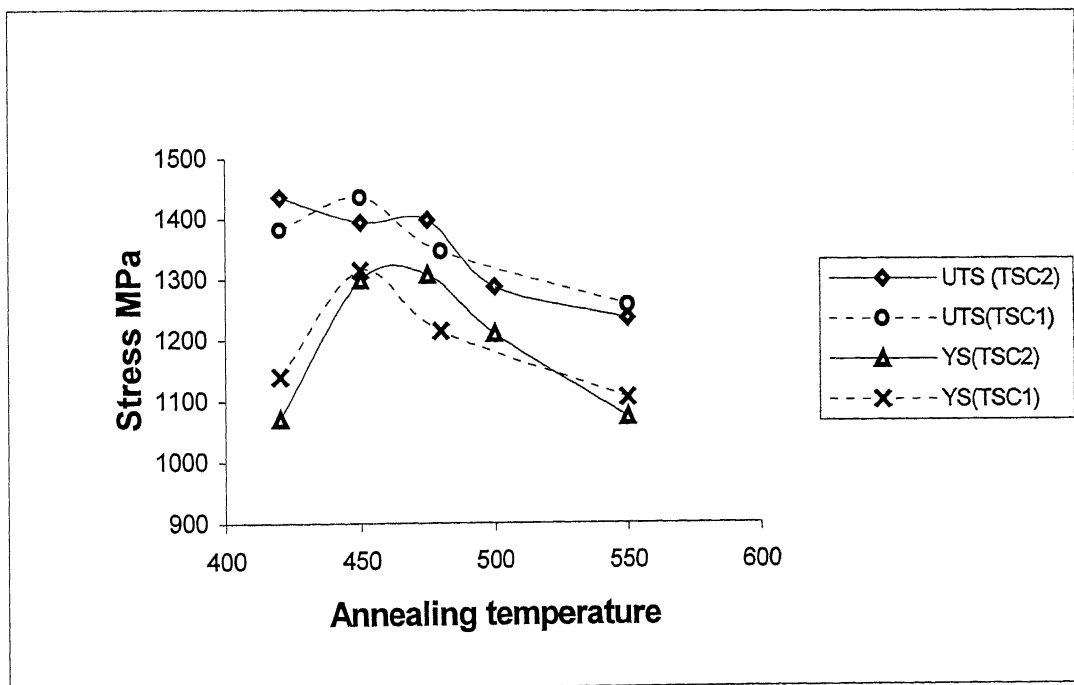


**Figure 4.20b:** Effect of annealing temperature on the strength of TSC1 and TSC2

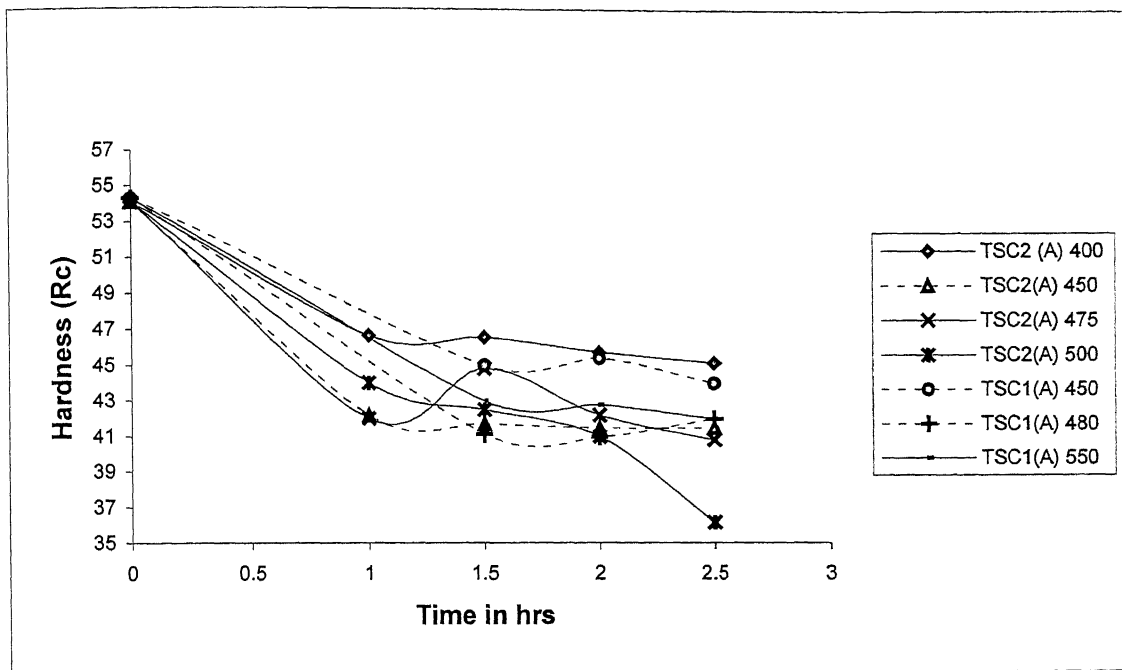


**Figure 4.20c:** Effect of Annealing temperature and Time on Hardness.

structure sensitive property, percentage reduction in area (%RA), values was very close. It can be seen from the table 4.5, that both the TSC conditions display a higher proof stress (around 9% more) and UTS (11.6% or more) compared with Q&T and air-cooled condition. From the figure 4.20 it is certain that at annealing temperatures in the range 450°-475°C the properties are maximum. Though the microstructures and hardness trend do not indicate the importance of variation in annealing temperature and time, the tensile test results positively indicate that annealing in the temperature range 450°-475°C for 1.5 hrs gives the best combination of tensile properties. More over the strength ductility combination is superior for TSC2 samples annealed at 450°C for 1.5 hrs, than TSC1 sample annealed under same conditions. From the table 4.5, it can be seen that the air-cooled samples showed maximum ductility compared to other conditions but the strength level was inferior. The percentage elongation (%E) for air-cooled samples was 42% more than for TSC samples and 32% more than in the Q&T condition. Along with this the percentage reduction in area (%RA) was 20% more than in TSC2 and 17.2 % more than in Q&T conditions.

The optimal tensile properties obtained in reference to TSC2A and Q&T conditions were compared and are shown in table 4.6. It was observed that the strength and the ductility obtained from the TSC2 material annealed at 450°C for 1.5 hrs was comparable to those of the Q&T material tempered at 550°C for 1.5 hrs. The representative engineering stress-strain curve for TSC and Q&T treatment are shown in figure 4.21. The curve does not display any sharp yield point. For the purpose of quantification of toughness, the area under the stress-strain curve up to the end of uniform elongation ( $U_T$ ) was calculated. The modulus of resilience ( $U_R$ ) of TSC2 condition was 12.4 % more than that for Q&T condition mainly because of its higher yield strength (table 4.6). But the plastic strain energy that pertains to the plastic range only ( $U_P$ ) for the TSC2 condition was only 80% of that for the Q&T condition. The total area under the stress – strain curve, which covers both the elastic and plastic ranges ( $U_T$ ) for the TSC2 condition (up to uniform elongation), was about 82% of the Q&T condition. So Q&T condition shows superior toughness properties than TSC2 annealed condition.



**Table 4.5** Tensile properties of different conditions

| Material Condition   | %Elongation (%E) | % Reduction in Area (%RA) | Ultimate Tensile Strength (UTS) MPa | Yield Strength MPa |
|--|------------------|---------------------------|-------------------------------------|--------------------|
| Air-cooled   | $19.55 \pm 2$    | $51.8 \pm 2$              | $1020 \pm 10$                       | $721 \pm 12$       |
| Two step cooling1 +annealing (TSC1)                              | $9 \pm 1$        | $44 \pm 1$                | $1437 \pm 15$                       | $1314 \pm 15$      |
| Two step cooling2 +annealing (TSC2)                              | $11.26 \pm 0.5$  | $41.34 \pm 1$             | $1395 \pm 20$                       | $1299 \pm 10$      |
| Quenched from the forging temp. and tempered at 700°C for 1.5hrs | $17.63 \pm 1$    | $54.35 \pm 3$             | $976 \pm 4$                         | $873 \pm 6$        |
| 650°C for 1.5hrs   | $15.3 \pm 4$     | $54.11 \pm 1$             | $1002 \pm 25$                       | $913 \pm 15$       |
| 550°C for 1.5hrs   | $13.13 \pm$      | $42.88 \pm 3$             | $1250 \pm 10$                       | $1185 \pm 20$      |

The strength of air-cooled samples was inferior to two-step cooled samples because of the reason that it had comparatively softer constituent phases. With 60% pearlite and remaining 40% proeutectoid ferrite the hardness is significantly less than what was obtained with two-step cooled samples, hence inferior strength levels but very high ductility was observed.

**Table 4.6** Comparison of toughness of optimal two-step cooled condition with optimal quenched and tempered condition.

| Material condition                                       | Modulus of resilience ( $U_R$ ), $\text{MJm}^{-3}$ | Area under the stress-strain curve up to the end of uniform elongation, ( $U_T$ ), $\text{MJm}^{-3}$ | Plastic strain energy up to the end of uniform elongation, ( $U_P$ ), $\text{MJm}^{-3}$ |
|--|--|--|---|
| Quenched and tempered at 550°C for 1.5 hrs               | 3  | 67   | 64  |
| Two-Step Cooling (TSC2) + Annealing at 450°C for 1.5 hrs | 4  | 55   | 51  |

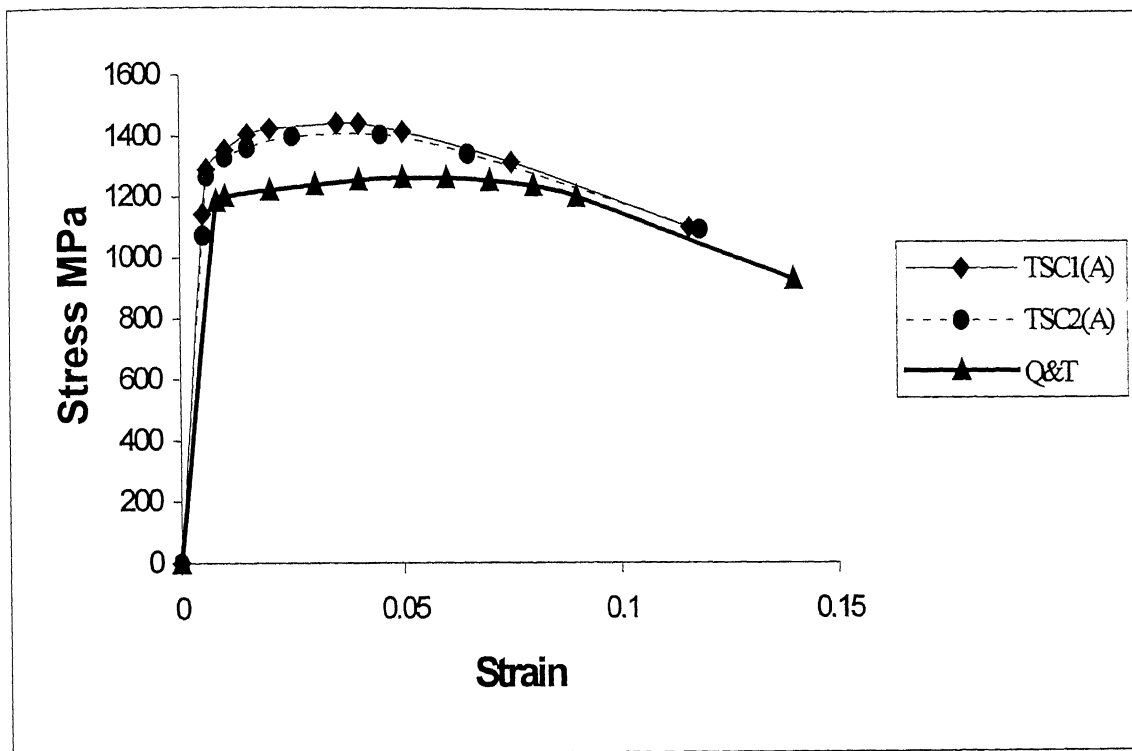


**Fig.4.21** Representative stress-strain curve of TSC and Q&T

The high strength levels observed in annealed TSC1 are because of the higher volume fraction of the harder phase bainite in TSC1 than in TSC2 as explained in section 4.2. It has already been stated in section 4.1.3 that annealed samples of TSC2 show higher ferrite content at almost the same hardness level with TSC1. The higher amount of bainite leads to lower ductility as is shown by the low percentage elongation values observed for TSC1 (table 4.5). TSC2 sample had higher amount of ferrite in it and hence larger percentage elongation values were obtained. The combination of ductility and tensile strength was better for TSC2 samples. Presence of higher ferrite content in TSC2 also leads to higher toughness obtained.

The effect of annealing temperature on the tensile properties is very significant. It was observed that TSC2 samples showed best strength-ductility property combination at 450°C when annealed for 1.5 hrs. If annealing temperature was changed from 450°C (increased or decreased) the tensile properties obtained were inferior. This can be explained with respect to the precipitation of vanadium carbides. During annealing the martensite in the structure decomposes to carbides and ferrite. The cementite present in the bainite coarsens with no other change in bainite. Vanadium carbides are preferentially precipitating in free ferrite and in bainitic ferrite during annealing, which causes secondary hardening. It is quite possible that maximum amount of fine vanadium carbide (VC) precipitates are present around 450°C. Below this temperature the volume of VC is not significant to cause any influencing secondary hardening. If the temperature is raised to 500°C, drop in strength levels was observed which could be because of the fact that in this temperature range the fine precipitate begin to coarsen and hence the drop in strength. So the maximum strength is observed in TSC2 samples when annealed at 450°C.

For studying the importance of position of the tensile samples in the rod, gage length of the tensile samples was decreased from 35 mm to 20 mm and tensile tests were performed on TSC1 samples annealed at 450°C for 1.5 hrs. It was found that there exists a scatter in the tensile properties along the length of the rod, which can be because of the inhomogeneity in the structure along the rod. It was observed that tensile samples taken from a distance of 10-18 cms from both ends of the rod showed slightly superior combination of strength and ductility. But the tensile properties of samples taken from

other positions along the rod were comparable, if not the same. Hence the inhomogeneity in hardness and structure along the rod does not significantly affect the tensile properties along the length of the rod.

## CHAPTER 5

### Conclusions

Some major conclusions that have resulted from the present investigation are

1. The variation in thermomechanical treatment resulted in different microstructures in the 38MnSiVs6 medium carbon microalloyed steel. The material that was continuously cooled in air after forging had ferrite-pearlite structure. The two-step cooled material had ferrite, lower bainite and a small amount of martensite. There was no retained austenite in the two-step cooled material.
2. The structure at the extreme end, of all the differently treated rods, was very fine. The fineness decreases gradually along the rod up to a certain distance and then it starts increasing gradually to the center of the rod.
3. The two-step cooled material that was forged at a lower finish forging temperature (750-850°C), TSC2 has a larger fraction of proeutectoid ferrite than TSC1, the two-step cooled material that was forged at a comparatively higher temperature (850-900°C).
4. The structure of TSC2 showed finer grains than TSC1 material.
5. The free ferrite content of the two-step cooled material was maximum at extreme end and it gradually decreases along the rod till a certain region and beyond that it again starts increasing up to the middle of the rod.
6. The two-step cooled material when annealed at different temperatures and for different time did not respond to change in the annealing cycle. The change in the annealing temperature above 400°C and beyond 1hr did not show any change in the optical and SEM microstructures observed.
7. Annealing of two-step cooled material resulted in an increase in the free ferrite in the structure along with coarsened cementite.
8. The use of thin plates for X-ray diffraction analysis did not account for the oriented structure and gave erroneous results.

9. TSC2 material showed better ductility strength relationship than TSC1 material.
10. Tensile properties of annealed two-step material are the best with annealing done at 450°C for 1.5 hrs.

### **Suggestions for Future Work**

1. Transmission electron microscopy should be used for the detailed study of two-step cooled microstructure.
2. X-Ray diffraction should be performed on powder samples to avoid the affect of orientation. Temperature factor should also be incorporated in the intensity equation.
3. The influence of deformation on the texture of material can be studied.

## References

1. D.J. Naylor, in Proc. Int. Conference *Microalloying in Steels*, Eds. J.M. Rodriguez-Ibabe, I. Gutierrez, B.lopez, Trans Tech Publications, Switzerland, (1998) 83.
2. Gonzalez-Baquet, R. Kasper and J. Richter, Steel Research 68 (1997) 61.
3. R. Kasper, I. Gonzalez-Baquet, N. Schreiber, J. Richter, G. NuBbaum and A. Kothe Steel Research 68 (1997) 27.
4. Gonzalez-Baquet, R. Kasper, J. Richter, G. NuBbaum and A. Kothe Steel Research 68 (1997) 534.
5. R. Kasper, I. Gonzalez-Baquet, J. Richter, G. NuBbaum and A.Kothe, Steel Research 68 (1997) 266.
6. G. Fourlaris, in Proc. Int. Conference *Microalloying in Steels*, eds. J.M. Rodriguez-Ibabe, I. Gutierrez, B.lopez, Trans Tech Publications, Switzerland, (1998) 427.
7. Sekine, in *Thermomechanical Processing of High Strength Low Alloy Steels*, Imao Tamura, Chiaki Ouchi, Tomo Tanaka, Hiroshi Sekini, Butterworths,1988.
8. Ouchi, in *Thermomechanical Processing of High Strength Low Alloy Steels*, Imao Tamura, Chiaki Ouchi, Tomo Tanaka, Hiroshi Sekini, Butterworths,1988.
9. R. Abad, B. Lopez, I.Gutierrez, in Proc. Int. Conference *Microalloying in Steels*, Eds. J.M. Rodriguez-Ibabe, I. Gutierrez, B.lopez, Trans Tech Publications, Switzerland, (1998) 427.
10. *STEEL, A Handbook for Materials Research and Engineering*, Volume1:Fundamentals, Springer-Verlag Verlag Stahleisen
11. G. Krauss, in: *Materials science and technology: Constitution and Properties of Steels*, Eds F. Brian Pickering, Vol 7(1984)
12. T. Ando, G. Krauss,), Acta Metall.29, (1981) 351.
13. H.I. Aaronson, in: *Decomposition of Austenite by Diffusional Process*: V. F. Zackay, H.I. Aaronson, (Eds.). New York: Interscience, (1962) 387-548.

14. H.I. Aaronson, C. Laird, K.R. Kinsmann: *Phase Transformations in Ferrous Alloys*, Eds. A.R. Marder, J.I. Goldstein, Warrendale, PA, TMS-AIME, (1970), 243
15. Reynolds, W.T., Enomoto, M., H.I. Aaronson, in: *Phase Transformation in Ferrous Alloys*, Eds. Marder, A.R., Goldstein, J.I. Warrendale, PA, TMS-AIME, (1984) 155-200
16. J.B. Gilmour, G.R. Purdy, J.S. Kirkaldy, *Metall Trans*, 3 (1972) 3213
17. R.F. Mehl, W.C. Hagel, in *Progress in Metal Physics*, Eds. B.Chalmers, R. King, New York: Pergamon Press, 74-134.
18. M.S. Wechsler, D.S. Lieberman, T. A. Read, *Trans. TMS-AIME*, 197 (1953) 1503.
19. F.B. Pickering, *Physical Metallurgy and the Design of Steels*, Applied Science Publishers, London, (1978).
20. J.S. Bowles and J.K. Mackenzie, *Acta Metall.*, 2, 129
21. B.A. Bilby, J.W. Christian, *J. Iron and Steel Institute*, 197 (1961) 122.
22. C.M. Wayman, *Introduction to the Crystallography of Martensite Transformations*, New York, MacMillan.
23. A.B. Greninger, A.R. Troiana, *Trans. TMS-AIME*, 185 (1949) 590.
24. A.R. Marder, G. Krauss, *Trans.ASM*, 60 (1967) 651
25. J.W. Christian, D.V. Edmonds, in: *Phase Transformations in Ferrous Alloys*: Eds.A.R. Marder, J.I. Goldstein, Warrendale, PA, TMS-AIME, 293-326.
26. R.F.Mehl, in *Hardenability of Alloy Steels*, Metal Park: ASM, (1939) 1
27. R.F. Hehemann, in *Phase Transformations*, Metals park, ASM, (1970) 397-432.
28. R.W.K. Honeycombe, *Steels Microstructure & Properties*, 81-115
29. R.M.K. Honeycombe and H.K.D.H. Bhadeshia, *Steels: Microstructure and Properties*, Second Edition, Edward Arnold, London, 1995, 83-123
30. A.K. Sinha, *Ferrous Physical Metallurgy*, Edward Arnold, 248
31. Y. Ohmori, H. Ohtsubo, Y.C. Jung, S. Okaguchi and H. Ohtani, *Metall. Mater. Trans*, Vol 25A (1994) 1981.
32. . M. Hillert, *Metall. Mater. TransactionsA*, Vol 25A, (1994) 1953
33. G. Spanos, *Metall. Mater. Trans*, Vol 25A (1994)1967



34. H.K.D.H. Bhadeshia, D.V. Edmonds, Metall. Trans, 10A (1979) 895.
35. K. Tsuzaki, A. Kodai, T. Maki, Metall. Mater. Trans, 25A (1994) 2009.
36. L.C. Chang, H.K.D.H. Bhadeshia, Mater. Sci. and Technol, 11 (1995) 03
37. L.C. Chang, H.K.D.H. Bhadeshia, Mater. Sci. and Technol, 12 (1996) 233.
38. Matsuzaki, H.K.D.H. Bhadeshia, Mater. Sci and T Technol, 15 (1999) 518
39. M. Hillert, G.R. Purdy, Scripta Metall. 32 (1984) 823
40. M. Hillert, G.R. Purdy, Scripta Mater. 43 (2000) 831
41. H.K.D.H. Bhadeshia, *Bainite in Steels*, Institute of Materials, London (1992)
42. B.D. Cullity, *Elements of X-Ray Diffraction*, Addison-Wesley, 1958.
43. F.H. Herbstein and J. Smuts, Acta Cryst. 17 (1964) 1331.
44. G. NuBbaum, J. Richter, A. Gueth, A. Kothe, R. Kasper and I. Gonzalez-Baquet, Mater Sci. Forum, 284-286 (1998) 443-450.
45. Sankaran, S., Subramanya Sarma, V., Kaushik, V. and Padmanabhan, K.A, Thermomechanical processing and characterisation of multiphase microstructures in a V-bearing medium carbon microalloyed steel. Proc. Int. Manufacturing Con. in China IMCC'2000, Hong Kong, 14-16 Aug. 2000